Physical modeling and simulation of electro-mechanical actuator-based TVC systems for reusable launch vehicles

Stefano Farì[a,*], David Seelbinder[a], Stephan Theil[a], Pedro Simplicio[b] and Samir Bennani[b]

[a]German Aerospace Center (DLR) - Institute of Space Systems - Navigation and Control Systems Department, Robert Hooke Straße 7, Bremen, Germany
[b]European Space Agency (ESA) - GNC, AOCS & Pointing Division, Keplerlaan 1, Noordwijk, The Netherlands

ARTICLE INFO

Keywords:
Thrust Vector Control
Electro-mechanical actuators
Reusable launch vehicles
Modeling and simulation
Modelica
Validation and Verification

ABSTRACT

This paper presents the high-fidelity physical modeling of a Thrust Vector Control (TVC) system operated by Electro-Mechanical Actuators (EMAs) for Reusable Launch Vehicles (RLVs). In contrast to simplified, often linear, models, high-fidelity physical models enable a better assessment of the actual system performance and a deeper verification of the on-board software robustness against disturbances, unmodeled dynamics or degradation. This aspect is essential to enable the reusability concept as driven by long-term reliability requirements. Moreover, critical systems like Fault Detection, Isolation and Recovery (FDIR) logic, whose robustness and efficacy are often difficult to prove, can be thoroughly tested without requiring hardware experiments with eventual invasive modifications for fault injections. This work captures the whole dynamics of the EMA and TVC components, including the power drive electronics, the electrical motor, and the mechanical transmission for the EMA, as well as the mechanical properties of the engine nozzle acting as a load. The resulting differential algebraic equation system is modeled in the Modelica acausal object-oriented modeling language. An ad-hoc framework is implemented to guarantee flexibility and modularity, which allows models with different fidelity levels to be easily exchanged to achieve the simulation objectives and needed accuracy level. The impact of the different models on the closed-loop TVC dynamics is analyzed in both the frequency and time domain, and then benchmarked with a realistic RLV mission. The results show that the high-fidelity physical models provide a better understanding of the more complex effects governing the TVC dynamics and can, in turn, effectively improve its requirement definition process.

© 2023. This manuscript version is made available under the CC-BY-NC-ND 4.0 license. It is the accepted version corresponding to the published article, which can be found here: 10.1016/j.actaastro.2023.11.038.

1. Introduction

The reliability of reusable launch vehicles is a key factor for making access to space industrially and commercially viable. SpaceX's Falcon 9 rocket has shown that a rocket first stage can be successfully recovered multiple times with an increasingly lower refurbishing period. On this track, other companies followed this example, like Blue Origin or Rocket Lab [1]. Several projects are also taking place in Europe, where companies and research centers are putting high efforts to consolidate a similar know-how [2, 3, 4, 5].

Reliability has to be proven to the best extent before proceeding to the actual physical tests. The Validation and Verification (V&V) of the onboard software is essential to guarantee robustness against disturbances, performance degradation or faults. Relying only on hardware experiments for product testing and software validation can have major disadvantages in terms of cost and complexity of the hardware-based experiment. High-fidelity models and simulations, on the other hand, can sometimes be an efficient and effective alternative to assess the flight software capabilities [6, 7].

*Corresponding author
stefano.fari@dlr.de (S. Farì); david.seelbinder@dlr.de (D. Seelbinder); stephan.theil@dlr.de (S. Theil); pedro.simplicio@ext.esa.int (P. Simplicio); samc1960@hotmail.com (S. Bennani)
ORCID(s): 0000-0001-5595-6905 (S. Farì); 0000-0003-4080-3169 (D. Seelbinder); 0000-0002-5346-8091 (S. Theil); 0000-0002-7808-4502 (P. Simplicio); 0000-0003-0282-9448 (S. Bennani)

The main motivation behind this work is the need of enabling better vehicle diagnostic and recovery algorithm testing. This includes Prognostic and Health Management (PHM) [8], on-board Fault Detection and Isolation (FDI) [9] or Fault-Tolerant Control (FTC) [10] systems. Injecting faults in hardware components, or significantly altering their dynamics, is often costly, invasive and requires ad-hoc test benches to be designed and implemented. For this reason, high-fidelity models and simulations are essential to evidence new component behavior and possible effects on mission performance. Based on this, suitable countermeasures can be evaluated and implemented.

The most widespread approaches for model-based FDI rely on linear synthesis models to predict the expected outputs and generate a differential signal, called 'residual'. The latter is then compared with an appropriate threshold to decide on the fault occurrence and/or severity. A residual is ideally zero when no fault is occurring and when the system dynamics matches the one of the synthesis model. However, the latter condition is never achieved in practice due to model mismatches and disturbances, which is why assessing FDI solutions using high-fidelity models is essential.

1.1. Background and objectives

This work focuses on the high-fidelity physical modeling of Thrust Vector Control (TVC) systems based on Electro-Mechanical Actuators (EMAs). In a launch vehicle, the TVC system provides the engine thrust pointing commanded by

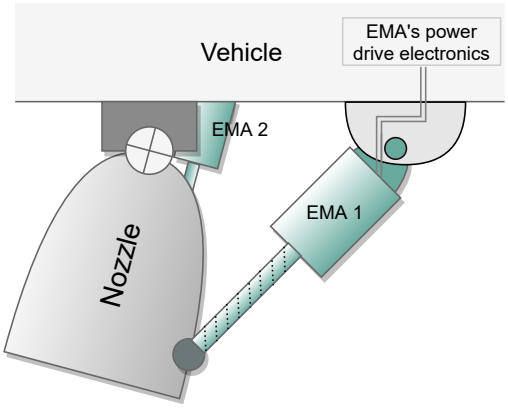

Figure 1: Simplified depiction of a TVC system maneuvered by two orthogonal electro-mechanical actuators.

the vehicle's control system to correctly steer it along the desired trajectory. The TVC system is normally assembled with a geometry that enables linear actuators to move the engine thrust exit point about a gimballing mechanism that guarantees the necessary rotational degrees of freedom (see Figure 1). To drive such a system, Electro-Hydraulic Actuators (EHAs) [11] or Electro-Mechanical Actuators (EMAs) [12] can be employed. It should be noted that in liquid-engine rockets the deflection typically involves the entire engine assembly, not just the nozzle. This distinction has significant implications for preventing structural fatigue phenomena and therefore plays a role in defining the frequency requirements for the actuators closed-loop. In the following, the terms 'engine' or 'nozzle' are often used interchangeably and refer, more generally, to the gimbaled load.

Electrical power drives are increasingly asked to replace fluid power drives: in aeronautics the ideal goal for more-electric aircraft is to remove hydraulic actuators as means for primary control and replace them with reliable EMAs [13, 14, 15]. Launch vehicles can benefit from such an implementation because a large fraction of mass, space, and cost can be saved with respect to conventional hydraulic actuators [11, 16]. EMAs have been successfully used, for example, in the expendable European VEGA rocket [17, 18, 19] over two decades of operational life, or in the more recent Electron rocket [12].

Concerning FDI solutions for EMAs, Balaban *et al.* [20] proposed a diagnostic algorithm based on an artificial neural network to diagnose EMA sensor faults and classify component failures, Della Vedova *et al.* [21] considers a model-based FDI method for the prognostics of EMAs using genetic algorithms, while Bennett *et al.* [22] and Ossmann [23] developed a model-based FDI approach based on linear synthesis techniques. More recently, a similar approach was applied to an EMA-based TVC system in Farì *et al.* [24].

EMAs rely on an electrical power source to suitably feed an electric motor, whose rotational motion is then converted into a linear motion via a nut-screw mechanism. Several power conversion stages are required to transition from the purely electrical domain to the linear mechanical one, while involving the thermal and magnetic domains as well. Although EMAs are widely known and adopted actuators in all engineering fields, accurately capturing their dynamical behavior is not trivial. The difficulty lies in the nonlinear characteristics affecting the power converters, such as the power drive electronics (PDE), the electric motor (EM) and the mechanical power transmission (MPT). They introduce higher-order dynamics and nonlinearities, like saturations, rate limits, backlash, dead-zones, and friction. Moreover, in launch vehicles the loads induced by their dynamics onto the actuators are not negligible.

For simulation, the employment of physical models represents a suitable solution: this means capturing the behavior of individual components interconnected via a "network" that follows the real system architecture. Nevertheless, this approach usually implies slower simulation times and a higher computational load; furthermore, it becomes more difficult to track down and objectively decompose the performance delivered by each software subcomponent. This choice must be therefore counterbalanced by a strategy to keep control on the complexity level of the entire model to simulate. Thus, it is necessary to balance the final model architecture versus the engineering needs. This is only possible with an incremental modeling strategy where each component has several implementations with different fidelity levels that can be accordingly exchanged.

In rockets utilizing gimbaled thrust, complex dynamics emerge from the interaction between the engine/nozzle, EMA and the rest of the vehicle. Orr *et al.* [25, 26] analyze this interaction with a specific focus on the effect of the components flexibility. The engine represents a considerable portion of the vehicle's total mass, especially as the propellant is depleted. This results, from the vehicle perspective, into engine-caused forces and torques acting on the vehicle body, causing an effect known as Tail-Wag-Dog (TWD). From the perspective of the engine, the opposite forces and torques are hereafter referred to as vehicle-induced loads. In the following, despite the components are assumed to be rigid, the use of acausal simulation techniques in conjunction with multibody models is instrumental because it inherently computes and resolves the overall "vehicle+engine" Differential-Algebraic Equations (DAEs) of motion without explicitly requiring the calculation of TWD and vehicle-induced action-reaction forces and torques (see *i.a.* [27]).

1.2. Contributions and outline

This work expands upon the following points:

1. the selection and implementation of EMAs physical models with different complexity levels and their integration into a TVC system architecture;

2. the adoption of an appropriate framework to enable an easy scalability of the fidelity levels per each component based on the simulation accuracy needs;

Table 1
Requirements for TVC simulation models implementation.

Requirements	
Realism	Genericity
Minimalism	Interfaces standardization
Ageing/faults inclusion	Parametrization
Power flows (a)causality	Complexity progressivity

3. the analysis of the impact of each of these models on the whole TVC dynamics in both the frequency and time domains.

Additionally, the first point has the extra benefit of allowing the introduction of specific EMA faults at component level, rather than artificially altering the model outputs based on an a-priori expectation on the fault consequences. This aspect makes possible to assess degradation based on a realistic fault propagation.

Maré *et al.* extensively investigated the aspects of modeling and simulating EMAs, with dedicated consideration to multidisciplinary effects including thermal characteristics, high-fidelity friction modeling, embedded control system design, sensing units, and stressed the importance of each modeling and simulation efforts for the designer from a system engineering perspective [13, 28, 29, 30, 31, 32]. In Fu *et al.* [33, 34], an approach for incremental virtual prototyping of EMAs is proposed. However, these works:

1. have not been conjugated to EMA-based TVC systems for expendable or reusable launch vehicles yet;

2. do not introduce a structured simulation framework where a formal implementation methodology can be used for the incremental-fidelity dynamic modeling and analysis of EMA-based TVC systems;

3. do not provide a dedicated frequency-domain analysis for a better perspective on the control design impact and/or for the requirements definition.

As for (1), the sophistication level reached by comprehensive TVC models in literature, like the one proposed in [35], is limited, because often targeted to the TVC control system synthesis only, and not on a deeper testing and verification level as well. Another reason for this is the confidentiality of such topic, that aims at protecting industrial assets or that is enforced by export control laws. Furthermore, to the best of the authors' knowledge, no study has so far addressed the creation of a TVC model that includes all the couplings, inertial effects, as well as reaction forces and torques arising from the interaction of all components. It is worth remarking that, although the methodology of this paper is tailored for RLV TVC systems, it can be adapted to other applications as well due to the generality of the configuration (vehicle, EMAs, load).

Considering issue (2), numerous multi-domain and system-level simulation packages are now available on the market. Given the modeling complexity, acausal modeling languages are a mandatory choice to achieve the requirements listed in Table 1. These effects are rarely addressed as a whole for TVC systems because of a lack of suitable approaches for models architecture, incremental modeling, and judicious model implementation. The object-oriented acausal modeling language Modelica is commonly used for advanced spacecraft modeling and simulation [36, 37, 38, 39]. This tool has already been applied to EMAs as well: Modelica libraries have been proposed in some works like van der Linden *et al.* [40] and Bozhko *et al.* [41]. Maré adopts Modelica to implement friction, backlash and preload for the mechanical transmission [31]. These efforts have been taken into consideration in this work and conjugated to achieve the proposed implementation and simulation requirements. Special consideration is given to models "replaceability" and overall packages encapsulations.

The remainder of the paper is structured as follows: Section 2 highlights the reasons why, for this type of problems, an object-oriented modeling approach is the ideal choice and, consequently, why the Modelica language is adopted. Section 3 introduces the main TVC components, while Section 4 describes the models adopted for the PDE, EM and MPT, as well as the whole TVC hardware implementation. Section 5 presents a TVC linear model and Section 6 the TVC embedded control system. Section 7 analyzes the linearized systems arising from the different implementations in the frequency domain. Section 8 shows the simulation results in the time domain for the EMA models in a standalone configuration and as integrated within a full end-to-end reusable launch vehicle simulator. Section 9 concludes the paper.

2. Physical object-oriented modeling for RLV's high-fidelity dynamic simulations

The state-of-practice environment for dynamic simulations, especially at industrial level, is Simulink, which is convenient for rapid prototyping, control systems design and for the numerous available tools and add-ons that potentially allow for the software testing, requirement checks, or Monte-Carlo campaign executions in one single development environment. However, Simulink is 'causal' or 'block-oriented', and its main limitation consists in the blocks having a unidirectional data flow. As such, certain relationship cannot be directly modeled. For example, electrical machines or gearboxes, both part of EMAs, may have a direct or indirect power flow: simulating this in a causal manner has several drawbacks, such that the implementation has to diverge from the actual physical phenomenon, while decreasing the models reusability. Furthermore, certain models requiring algebraic constraints, *e.g.* multibody systems become unmanageable within Simulink. Lastly, when the models include cross-coupling between different physical domains, models cannot be easily interchanged. Note that the Simulink Simscape® commercial add-on package also allows acausal modeling.

```
partial model Sensor
   Flange_a shaft; // input connector
   RealOutput w;   // output connector
end Sensor;

partial model SystemArchitecture
   replaceable Sensor sensor constrainedby Sensor;
   // <...> Other declarations and dyn. equations
end SystemArchitecture;

model BaseSystem
   extends SystemArchitecture(
       redeclare IdealSensor sensor);
   // <...> Other redeclarations or modifications
end BaseSystem;
```

Figure 2: Example of the architecture-driven approach. A partial model `SystemArchitecture` builds up the system architecture, while `BaseSystem` model defines the models populating its replaceable components. In this case `IdealSensor` model (not shown) is replacing `Sensor`.

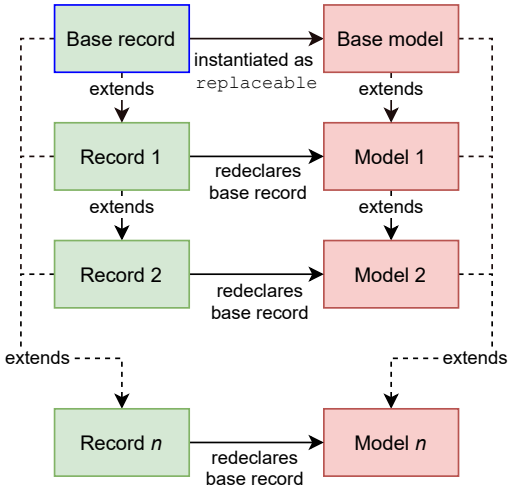

Figure 3: *Record* classes used for data component handling within models.

It is however not considered because it has a limited, non-modifiable selection of components, which do not fulfill our modeling needs.

The free acausal modeling approach adopted by the Modelica language, on the other hand, is based on equations instead of assignment statements and allows to overcome these limitations and give additional modeling flexibility. The object-orientation [42, 43] enables: (1) a clear representation of physical meaning within an object-oriented structure; (2) modularization and component reuse features, allowing a greater model adaptiveness against changes. The class concept and inheritance property are the keys for reuse of modeling knowledge in Modelica. The 'inheritance through modification' property via the so-called 'modifiers' makes reusing the models even more straightforward and the implementation concise. A free Modelica Standard Library (MSL) exists [44] to facilitate the user with basic components belonging to different physical domains.

The full EMA and TVC component models are integrated within the Vertical Landing Vehicles Library (VLVLib) developed by DLR [7]. The library is built over certain principles that exploit the Modelica features in order to allow the user to easily create new vehicles with a specific selection of dynamic effects without having to re-implement the interfaces between components. The most important adopted modeling practices are hereafter briefly recalled.

Encapsulation The models are contained within several nested packages, which are declared as `encapsulated`, guaranteeing that the class names lookup stops at the boundary of the package itself for implementation cleanliness.

Architecture-driven approach The library is designed in a modular and flexible way such that the fundamental subsystem interfaces have been pre-connected. The final model implementation is obtained by selecting a specific implementation (model) for each subsystem, after guaranteeing that all implementations are "plug-compatible," *i.e.* have the same interfaces. This is possible in Modelica using the `replaceable`/`redeclare` properties. An example is shown in Figure 2.

Matlab/Simulink integration The developed models can be compiled and exported as S-functions or Functional Mockup Units (FMUs). As such: (1) inputs/outputs are defined as causal connectors; (2) the implementation seeks to avoid the replication of functions often implemented in Matlab/Simulink (*e.g.* frame conversions, environment modeling, etc).

Information propagation The interfaces between models, given the numerous quantities involved, can make modifications to the root vehicle layer tedious and error-prone. For this reason, the connectors are often grouped within *expandable connectors* (or *busses*)[1].

Data handling Modelica *records* are special classes meant to functionally group data. They can also extend other *records* and eventually modify them to create a specific hierarchy which helps to manage the large amount of data, *i.e.* model parameters. A model instantiating a *record* is allowed to access its data. This is relevant when models with different complexity are to be used, therefore one specific record can be assigned to each model. Different record/model inheritance combinations enable a big modeling flexibility while guaranteeing that each model accesses the minimal set of data needed for execution. This concept is depicted in Figure 3.

[1] A Modelica connector declared as expandable has no minimum requirement for information to be carried on the bus. The bus can thus be expanded to include additional information without restrictions on the connector types.

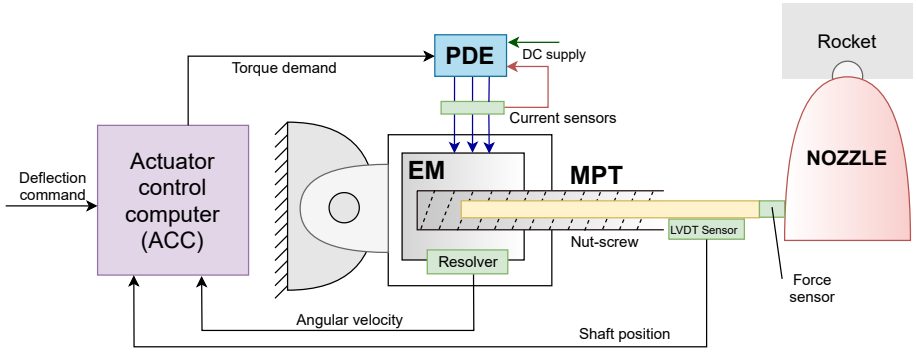

Figure 4: Representation of an EMA-based TVC architecture.

3. EMA-based TVC system description

To properly steer the engine's thrust vector direction, the TVC must be able to tilt the engine's nozzle for the correct pointing as commanded by the GNC system. For this reason, the engine is commonly mounted on a gimbal system and maneuvered by two linear actuators in a closed kinematic chain, designed to comply with the EMA load limits, as well as the required speed and maximum displacement operational domains.

The EMA-based TVC system comprises the following hardware:

- the engine with its structural supports, anchorage points and mechanical joints;
- a DC power source and the conditioning power electronics;
- the embedded actuator control computer (ACC), in charge of controlling the EMA position to achieve the commanded TVC deflections;
- two EMAs to physically move the engine nozzle.

More closely, an EMA is composed by four essential components, depicted in Figure 4:

- the power drive electronics (PDE), that manage the power flow between the electrical supply and the electric motor;
- a 3-phase Permanent Magnet Synchronous Motor (PMSM), hereafter recalled as electric motor (EM), to obtain a rotational motion from the electrical power;
- a mechanical power transmission (MPT) stage to convert the motor rotational motion into a linear one;
- sensors of EM current and rotational speed, stroke position (Linear Variable Differential Transformer) and force (if necessary).

4. Modeling of the EMA components physical effects

In this Section, the modeling of MPT, EM and PDE is tackled. For each, complexity levels labeled with L[1-n] are developed with increasing fidelity, as shown in Table 2. A TVC linear model (adoptable for control or model-based FDI synthesis purposes) is also developed and introduced in Section 5.

At this stage, the components not related with the EMA are modeled in a simple form. The electrical power lines and batteries are considered as ideal (no voltage drops nor discharge effects). The load (nozzle) dynamics includes only the inertial effect and the gimballing spring-damper mechanism (see Section 5). Since this work is not tailored to a specific vehicle TVC system, no assumption is made on the magnitude of the spring-damper constants. However, in some cases they may be considered negligible, like in liquid-propelled rockets.

In the discussion that follows, the modeling is treated as uni-dimensional (1D with translation/rotation domain only). This does not impede the models extension to a three-dimensional (3D, multibody) case; the approach to achieve this is explained in Appendix A, where all the implementation details using Modelica are explored.

4.1. Mechanical Power Transmission modeling

The role of the MPT is to convert the electric motor rotational motion into a linear one. The considered MPT relies on a planetary roller-screw mechanism. Normally this solution is adopted instead of the ball-screw mechanism to maximize the load that the actuator can withstand, at the cost of slightly decreasing its efficiency [33].

This study considers a direct-drive linear EMA. The VEGA launch vehicle has, for instance, adopted this solution [19]. Despite a geared-drive configuration enables larger speed-torque envelopes, often reduces motor complexity and saves mass, the direct-drive EMA integrates the motor rotor with the rotating nut-screw, which has several advantages: a higher geometrical integration potential due to the inherent spacial compactness, friction and backlash effects are reduced, and efficiency, stiffness and reliability are higher. At the same time, the flexibility of design, price and drive

Table 2
EMA modeling overall architecture matrix, showing the different dynamics included into each component implementation.

Component	Effect	Linear model	MPT- L1	MPT- L2	MPT- L3	MPT- L4	MPT- L5	MPT- L6	EM- L1	EM- L2	EM- L3	PDE- L1	PDE- L2	PDE- L3	PDE- L4
MPT	Basic transmission	✓	✓	✓	✓	✓	✓	✓	-	-	-	-	-	-	-
	Simple efficiency	✓	×	✓	×	×	×	×	-	-	-	-	-	-	-
	Structural compliance	✓	×	✓	✓	✓	✓	✓	-	-	-	-	-	-	-
	Screw mass	×	×	×	✓	✓	✓	✓	-	-	-	-	-	-	-
	Viscous friction	×	×	×	✓	✓	✓	✓	-	-	-	-	-	-	-
	Coulomb+Strickbeck friction	×	×	×	×	✓	✓	✓	-	-	-	-	-	-	-
	Load-dependent friction	×	×	×	×	×	✓	✓	-	-	-	-	-	-	-
	Backlash	×	×	×	×	×	×	✓	-	-	-	-	-	-	-
EM	External torque to rotor inertia	✓	-	-	-	-	-	-	✓	×	×	-	-	-	-
	PMSM dynamics	×	-	-	-	-	-	-	×	✓	✓	-	-	-	-
	Friction and other losses	×	-	-	-	-	-	-	×	×	✓	-	-	-	-
PDE	No dynamics	✓	-	-	-	-	-	-	-	-	-	✓	×	×	×
	Second order current dynamics	×	-	-	-	-	-	-	-	-	-	×	✓	×	×
	3-phase dynamics	×	-	-	-	-	-	-	-	-	-	×	×	✓	✓
	Inverter dynamics	×	-	-	-	-	-	-	-	-	-	×	×	×	✓

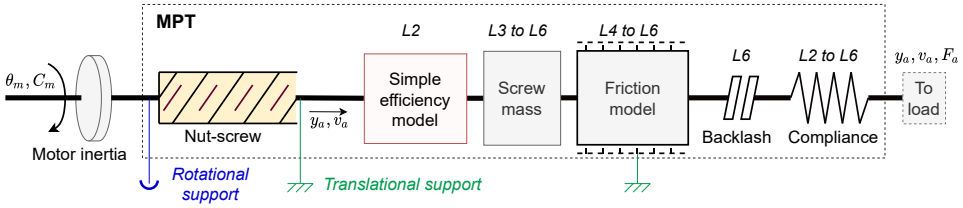

Figure 5: Simplified synoptic model for the MPT component.

Table 3
Main interface quantities of the MPT models.

Interface	Models	Quantity
Motor torque	all	C_m
Motor rotor position	all	θ_m
Stroke transmitted force	all	F_a or F'_a
Stroke position/velocity	all	y_a,v_a

electronics complexity remain comparable. From the dynamics point of view, a direct-drive architecture also avoids the unbalance present in a "deported motor" design where gearing mechanisms are present and shifted with respect to the actuator motion axis. For these reasons, gearing elements are not modeled in this work.

The model interfaces are summarized in Table 3. In Figure 5 a synoptic representation of the implemented parts of all MPTs is shown.

4.1.1. MPT-L1

The MPT-L1 model considers a perfect conversion of the motor torque, angular speed and angular displacement into a force, linear velocity and linear displacement, respectively. This can be expressed as:

$$y_a = L_g \theta_m, \tag{1}$$

$$v_a = L_g \omega_m, \tag{2}$$

$$F_a = L_g^{-1} C_m, \tag{3}$$

where y_a and v_a are the stroke displacement (from its neutral position) and velocity, θ_m and ω_m the motor rotor angular position and velocity, F_a the applied force to the load, C_m the electric motor torque, and L_g the nut-screw transmission ratio (rotational to translational). The latter can be obtained from

$$L_g = \frac{p}{2\pi}, \tag{4}$$

with p being the lead of the screw.

4.1.2. MPT-L2

This model extends MPT-L1 with a compliance effect. This can be seen as adding a spring dynamics after the translation of the rotational motion into a linear one. This model is meant to capture the effect of the equivalent structural elasticity of interconnection elements between the EMA and the nozzle. Therefore, the elastic force can be expressed as

$$F_e = k_s(y_a - y_e) \tag{5}$$

where k_s is the spring coefficient and y_e the translation of the nozzle which for small deflection angles can be obtained as

$$y_e = L_a \beta, \tag{6}$$

with β being the nozzle angular deflection for the considered EMA and L_a the actuator lever arm about the gimbaling point.

The effect of the load on the motor torque can be captured with F_e; furthermore, a mechanical efficiency factor η_e is introduced. As a result, the load torque to the motor can be expressed as

$$C_{m,\text{load}} = L_g F_e / \eta_e. \tag{7}$$

This yields to the new motor torque expression:

$$C'_m = C_m - C_{m,\text{load}}. \tag{8}$$

4.1.3. MPT-L3

Here the screw mass inertial dynamics is introduced and the efficiency factor is replaced with an explicit viscous friction implementation where the friction force is:

$$F_f = v_a \bar{F}_p \tag{9}$$

with F_f being the viscous friction force and $\bar{F}_p$ its force coefficient. This implies that the mechanical efficiency is not penalized at motor torque level, but at the applied force to the load, now being:

$$F'_a = L_g^{-1} C'_m - F_f - m_s \dot{v}_a, \tag{10}$$

with m_s being the additional screw mass.

4.1.4. MPT-L4

The viscous friction model from MPT-L4 is expanded by adding the Coulomb and Stribeck [45] effects. The friction F_f in Equation (9) can be then substituted with

$$F'_f = \left(\bar{F}_{cl} + |v_a|\bar{F}_p + \bar{F}_{st} e^{(-|v_a|/v_{\text{ref}})}\right) \text{sign}(v_a), \tag{11}$$

where $\bar{F}_{cl}$ is the Coulomb friction force coefficient, $\bar{F}_{st}$ and v_{ref} are the Stribeck force coefficient and reference speed respectively.

4.1.5. MPT-L5

In linear mechanical power transmissions, the dependence of friction on load is generally much greater than its dependence on velocity [29]. For this reason, the friction model is further enhanced considering a load-dependent component:

$$\begin{aligned} F''_f = \big[&\bar{F}_{cl} + |v_a|\bar{F}_p + \bar{F}_{st} e^{(-|v_a|/v_{\text{ref}})} \\ &+ |F_L|(a_1 + a_2 \text{sign}(F_L v_a))\big] \text{sign}(v_a), \end{aligned} \tag{12}$$

where a_1 and a_2 are two parameters regulating the dynamics of the new load-dependent friction term and F_L the load force. The implementation of a Modelica component capturing the load-dependent friction is shortly explained in Appendix B.

Table 4
Main interface quantities of the EM models.

Interface	Models	Quantity
Motor electromagnetic torque	L1	C_{em}
Three-phase stator voltages	L2, L3	$v_{s,1\text{-}3}$
Three-phase stator currents	L2, L3	$i_{s,1\text{-}3}$
Motor angular position/velocity	L1, L2, L3	θ_m, ω_m
Motor torque to the load	L1, L2, L3	C_m

4.1.6. MPT-L6

Lastly, the backlash effect with mechanical preload is introduced. Backlash is a "lost motion" happening within a mechanical transmission component, whereas preload is an elastic force occurring "while the motion is lost" to force the mechanics to always be in contact and achieve responsiveness [44, 46]. Formally, the two combined effects (backlash and preload) can be captured by a length-less component with the positions of its terminals expressed as x_1 and x_2, and whose produced elastic force is

$$F_{bl,e} = \begin{cases} k_{bl}(x_r - x_0), & x_r > x_0 \\ 2k_{\text{pre}} x_r, & |x_r| \le |x_0| \\ k_{bl}(x_r + x_0), & x_r < x_0 \end{cases} \tag{13}$$

where $x_r = x_2 - x_1$ is its relative displacement, x_0 is the backlash displacement, and k_{pre} the preload spring constant. At the same time, the damping force is similarly expressed as

$$F_{bl,d} = \begin{cases} \min(F_{bl}, d_{bl} v_r), & x_r > x_0 \\ 0, & |x_r| \le x_0 \\ \max(-F_{bl}, d_{bl} v_r), & x_r < -x_0 \end{cases} \tag{14}$$

where $v_r = \frac{d}{dt}(x_r)$ and d_{bl} is a damping coefficient. The $\max(\cdot)$ and $\min(\cdot)$ operators are necessary to bound $F_{bl,d}$ and avoid the "pulling/sticking" nonphysical effect when the damper torque becomes larger than the spring torque and with opposite sign. Forces $F_{bl,e}$ and $F_{bl,d}$ act as a spring-damper system in series with the structural compliance defined in Equation (5), so $F_{bl,e} + F_{bl,d}$ must equalize the actuation force.

4.2. Electric Motor modeling

The considered electric motor is a magnetically isotropic[2] Permanent Magnet Synchronous Machine (PMSM). This type of machines adopts permanent magnets to have a number of pole pairs fixed with the rotor that can be employed to generate an electromotive torque when a suitable magnetic flux is generated at the stator. Thus, the EM physical principles are the combination of effects acting in different physical domains: electrical, magnetic and mechanical. The model interfaces are reported in Table 4. Synoptic representations for EM-L1 and EM-L2/EM-L3 are given in Figures 6 and 7, respectively.

[2]The inductances do not depend on the rotor angular position.

4.2.1. EM-L1

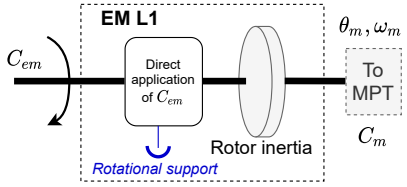

Figure 6: Simplified synoptic model for the EM-L1.

This is the simplest model, where the dynamic is represented by the rotor moment of inertia. This can be expressed as

$$C_m = C_{em} - J_r \dot{\omega}_m, \tag{15}$$

where J_r is the rotor moment of inertia and C_{em} the required motor electromagnetic torque.

4.2.2. EM-L2

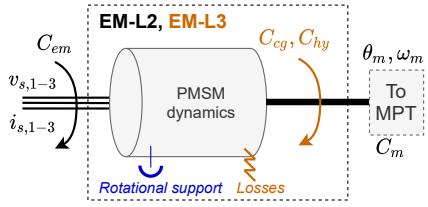

Figure 7: Simplified synoptic model for the EM-L2 and -L3.

The PMSM can be described considering the stator phases. The three-phase equations of an isotropic PMSM can be written as:

$$v_{s,1} = R_m i_{s,1} + \dot{\Psi}_{s,1}, \tag{16}$$
$$v_{s,2} = R_m i_{s,2} + \dot{\Psi}_{s,2}, \tag{17}$$
$$v_{s,3} = R_m i_{s,3} + \dot{\Psi}_{s,3}, \tag{18}$$
$$\Psi_{s,1} = L_m i_{s,1} + \Psi_{pm}(\theta_m), \tag{19}$$
$$\Psi_{s,2} = L_m i_{s,2} + \Psi_{pm}(\theta_m - \tfrac{2}{3}\pi), \tag{20}$$
$$\Psi_{s,3} = L_m i_{s,3} + \Psi_{pm}(\theta_m - \tfrac{4}{3}\pi), \tag{21}$$

where $v_{s,1-3}$ and $i_{s,1-3}$ are voltages and currents per phase, R_m and L_m are the stator resistance and inductance respectively, $\Psi_{s,1-3}$ is the magnetic flux per phase, Ψ_{pm} is the flux linked with the stator due to the permanent magnets depending on the rotor position θ_m. The expression for Ψ_{pm} is:

$$\Psi_{pm} = \bar{\Psi}_{pm} \cos(\theta_m), \tag{22}$$

with $\bar{\Psi}_{pm}$ the permanent magnets flux constant. By transforming Equations (16) to (22) using space phasors [47] and by introducing

$$\hat{\Psi}_{pm} = \sqrt{3/2}\bar{\Psi}_{pm}, \tag{23}$$

we can express the above equations in a stationary reference frame[3]; this transforms the three-phase machine into a two-phase one, equipped with two windings fixed with the stator and orthogonal to each other, expressed as d ('direct') and q ('quadrature'):

$$v_d = R_m i_d + \dot{\Psi}_d - \dot{\theta}_m L_m i_q \tag{24}$$
$$v_q = R_m i_q + \dot{\Psi}_q + \dot{\theta}_m L_m i_d + \dot{\theta}_m \hat{\Psi}_{pm} \tag{25}$$
$$\Psi_d = L_m i_d + \hat{\Psi}_{pm} \tag{26}$$
$$\Psi_q = L_m i_q. \tag{27}$$

The expression of the torque [47] for such a machine is given by

$$C_{em} = n_p \hat{\Psi}_{pm} i_q = k_t i_q, \tag{28}$$

where n_p is the number of pole pairs and k_t called as motor torque constant. The equation justifies how, in the control strategy only the quadrature current is used to produce a torque[4].

4.2.3. EM-L3

The most advanced EM-L3 model replicates EM-L2 with the addition of: 1. friction losses; 2. core losses (eddy current and hysteresis losses); 3. permanent magnet losses; 4. cogging torque. For consistency, their equations follow those used the Modelica Standard Library PMSM losses,[5] with the exception of the hysteresis and cogging torques. The overall motor torque balance becomes

$$C'_m = C_{em} - J_m \dot{\omega}_m - C_{\text{loss}}, \tag{29}$$

where C_{loss} term groups the dissipation and disturbance torques (friction, eddy currents, permanent magnet losses, cogging and hysteresis torques):

$$C_{\text{loss}} = C_{\text{fr}} + C_{\text{core}} + C_{\text{mg}} + C_{\text{cg}} + C_{\text{hy}}. \tag{30}$$

Note that the copper losses (Joule effect) are included already in the PMSM dynamics.

Friction losses The friction torque can be defined as:

$$C_{\text{fr}} = \begin{cases} C_{\text{fr,ref}} \left(\dfrac{|\omega_m|}{\omega_{\text{fr,ref}}} \right)^a \text{sign}(\omega_m) & \text{for } |\omega_m| > \omega_{\text{lin}} \\ C_{\text{fr,ref}} \dfrac{\omega_m}{\omega_{\text{lin}}} & \text{otherwise} \end{cases} \tag{31}$$

where $C_{\text{fr,ref}}$ and $\omega_{\text{fr,ref}}$ are the reference torque and speed at which the power loss is defined, a is a coefficient depending on the machine ventilation, and $[-\omega_{\text{lin}}, +\omega_{\text{lin}}]$ defines the angular speed range in which the losses are linearly dependent on the velocity.

[3] One axis has the same direction of the first winding magnetic axis.

[4] The direct current can be exploited for field weakening operations, but this goes beyond the objectives of this paper.

[5] More specifically, `Electrical.Machines.Losses` sub-package.

Core losses The penalizing torque due to eddy currents can be defined as:

$$C_{\text{core}} = P_{\text{core,ref}} \frac{(v_{s,1\text{-}3}/v_{\text{core,ref}})^2}{\omega_m} \tag{32}$$

where $v_{s,1\text{-}3}$ is the actual stator voltage per phase, while $P_{\text{core,ref}}$ and $v_{\text{core,ref}}$ are the reference power loss and the relative velocity at which it occurs, respectively.

Magnetic hysteresis generates an energy loss that directly depends on the motor electrical frequency. The produced disturbance torque [47] is:

$$C_{\text{hy}} = k_{hy} B_m^{\gamma} \omega_m, \tag{33}$$

where k_{hy} is the hysteresis constant, γ the Steinmetz constant [47] (generally between [1.5, 2.5]) and B_m the magnetic flux density.

Permanent magnet losses The permanent magnet losses are modeled depending on current and speed. They are included via an equivalent braking torque at the shaft [33]. The permanent magnet loss torque is

$$C_{\text{mg}} = \frac{P_{\text{mg,ref}}}{\omega_{\text{mg,ref}}} \left(c + (1-c) \left(\frac{i_{\text{s,RMS}}}{i_{\text{mg,ref}}} \right)^b \right) \left(\frac{\omega_m}{\omega_{\text{mg,ref}}} \right)^c \tag{34}$$

where $i_{\text{s,RMS}}$ is the Root-Mean-Square (RMS) value of the stator currents, the parameter c governs the dependency of the losses to the current. Parameters $P_{\text{mg,ref}}$, $i_{\text{mg,ref}}$ and $\omega_{\text{mg,ref}}$ define the reference power loss at a defined current and speed, while b and c alter the dependency of the output torque on the current and angular velocity.

Cogging torque During the motor rotation, the magnetic field around it changes and generates a torque ripple called cogging torque, as the rotor magnet moves between stator teeth [48]. Modeling this effect can be important because it depends on the motor velocity, which may generate detrimental vibrations and even excite the natural mechanical frequencies of an EMA. In this work, the latter aspect is not analyzed. To capture the cogging torque, an equivalent expression can be used where C_n is the rated motor torque and λ a cogging factor (usually relatively small):

$$C_{\text{cg}} = \lambda C_n \sin(n_p \theta_m). \tag{35}$$

4.3. Power Drive Electronics modeling

Modeling the PDE is important to capture voltage/current saturation and dynamical limits, as well as power losses. The role of the PDE is to provide the electric motor with the right power, thus the right voltage and current modulation from the vehicle electric bus supply. Launch vehicles employing a EMA-based TVC normally provide a dedicated high-level electrical power bus. Four PDE models are provided. The model interfaces are shown in Table 5.

Table 5
Main interface quantities of the PDE models.

Interface	Models	Quantity
Motor torque demand	L1, L2	C^*
Motor angular position/velocity	L3, L4	θ_m, ω_m
Motor electromagnetic torque	L1, L2	C_{em}
Three-phase stator voltages	L3, L4	$v_{s,1\text{-}3}$
Three-phase stator currents	L3, L4	$i_{s,1\text{-}3}$

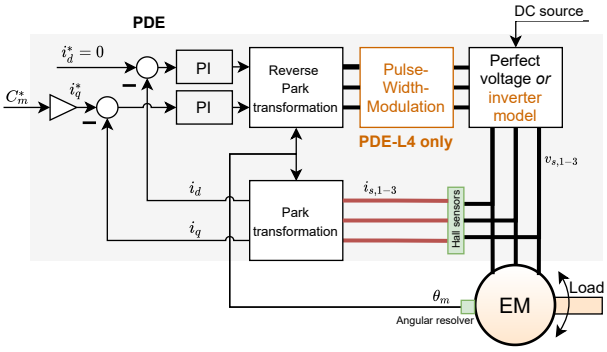

Figure 8: Schematic of the Field-oriented control for a 3-phase motor. The inverter model and the presence of the PWM depends on whether PDE-L3 or PDE-L4 is chosen.

Note that the PDE is not involved in the physical torque realization; inputting a torque instead of a current setpoint is an arbitrary modeling design choice, since the dependency between current and torque can be approximated via the introduced parameter k_t.

4.3.1. PDE-L1

The commanded torque C_m^* is transferred directly to the output C_{em}. There is no dynamics introduced.

4.3.2. PDE-L2

This model is meant to introduce the simplest possible current dynamics, while being used with EM-L1 (where only the inertial mechanical properties are modeled). Therefore, considering Equations (25), (27) and (28) it can be approximated with a first order transfer function:

$$I_q(s) = \frac{1}{L_m s + R_m} V_q(s). \tag{36}$$

The input voltage $V_q(s)$ is regulated by a PI controller with output saturation to respect the physical voltage limits and including a anti wind-up action. The need of a PI controller is common and arises from the aforementioned approximation, *i.e.* from the last two terms Equation (25), whose contribution is intended as disturbance for control design. The integral and proportional gains can be set to cancel the pole in (36) and have an arbitrarily fast dynamics.

4.3.3. PDE-L3

Here, the three-phase dynamics is accounted for, therefore the rotor position feedback is needed to properly employ the Park transformation. Two current closed loops are designed for both the direct and quadrature axes. The direct current setpoint i_d^* is set to zero, since it does not directly contribute to the torque realization. The input torque setpoint is transformed into the quadrature current $i_q^* = C_m^*/k_t$ that constitutes the reference for the current closed loop, as shown in Figure 8. The direct and quadrature controllers output the respective reference voltages, v_d^* and v_q^*. These are finally back-transformed into three-phase via a reverse Park transform and fed into a perfect voltage source representing the inverter dynamics for operating the EM. The currents i_d and i_q are obtained via ideal Hall sensors at the inverter output after a Park transformation.

4.3.4. PDE-L4

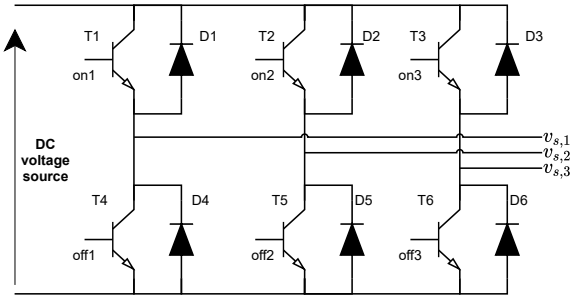

Figure 9: A simplified typical inverter bridge circuit. With 'T' and 'D' are the transistors and diodes, whereas 'on/off' labels denote the antagonist PWM signals per phase.

PDE-L4 model adds the Pulse-Width-Modulation (PWM), shown in orange in Figure 8, and inverter dynamics, with respect to PDE-L3 implementation. The inverter (Figure 9) adopts high-frequency switching of transistors to generate a voltage waveform that is naturally low-pass filtered by the EM. The transistors type is normally selected as a compromise between reachable switching frequency and the tolerated peak currents when activated. Examples are thyristors, BJTs, IGBTs or MOSFETs. Each transistor has an anti-parallel diode to obtain a fully functional switch for energy recovery.

The PWM on/off signal is generated by taking the direct and quadrature voltage outputted by the current controller and obtaining a space phasor. It is then possible to use the Space Vector Pulse-Width-Modulation technique (SVPWM) [47] to generate the on/off signals to be employed for opening/closing the transistors.

Both diodes and transistors are subject to losses:

- on-state conduction losses: they are due to the diodes and transistors on-state resistances. Their voltage drop has a generic expression:

$$v_{\mathrm{t/d}} = v_0 + R_{\mathrm{on}} i_{\mathrm{t/d}}, \tag{37}$$

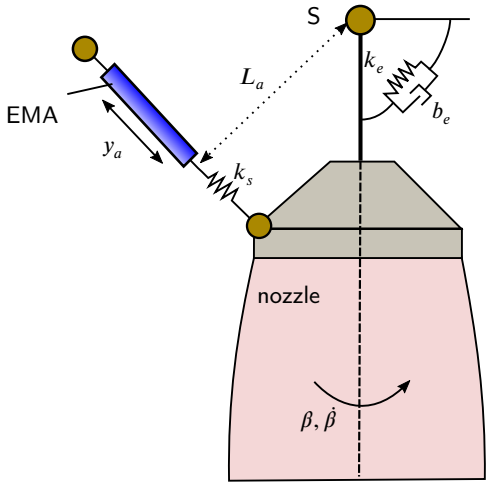

Figure 10: TVC system for linear modeling.

where v_0 is a static forward voltage drop, R_{on} the on-state resistance and $i_{\mathrm{t/d}}$ the operating current of either the transistor or diode.

- off-state blocking (leakage) losses: similarly, there exist also a voltage drop at off-state. It can normally be neglected due to the small quantities involved.
- turn-on/turn-off switching losses: during switching, a phase lag between current and voltage takes place. Normally it is about 10^{-7}s. Although relevant for energy losses analyses, it is hereafter neglected.

5. Linear TVC model

For algorithm synthesis techniques employing linear models, a TVC system state-space representation must be obtained. Hereafter, each gimbaling direction is considered independent from the other. Figure 10 depicts this architecture. The nozzle revolutes about a gimbal point S, where a rotational spring-damper mechanism with parameters k_e and b_e is applied. The EMA is connected to the nozzle via another spring and damper which encompass the anchor and rigging stiffness into an equivalent spring (with constant k_s). The stroke displacement y_a is considered as zero when $\beta = 0$. The sign of β depends on the EMA placement; in this study, it is considered that a positive EMA stroke displacement induces a positive gimbal angle. The state space equations of the system are:

$$\begin{aligned}
\dot{x}_1 &= x_2 \\
\dot{x}_2 &= -\alpha(k_e + L_a^2 k_s)x_1 - b_e \alpha x_2 + \alpha k_s L_g L_a x_3 \\
\dot{x}_3 &= x_4 \\
\dot{x}_4 &= J_m^{-1}\left(L_g k_s L_a \eta_e^{-1} x_1 - L_g^2 k_s \eta_e^{-1} x_3 \right. \\
&\quad \left. - b_m x_4 + u_1 + u_2\right)
\end{aligned} \tag{38}$$

Table 6
Inputs, outputs and states of the TVC linear state-space model.

	Inputs	Unit
u_1	EM torque	Nm
u_2	Vehicle-induced torque to the EM	Nm
	State	**Unit**
x_1	Gimbal deflection angle	rad
x_2	Gimbal deflection speed	rad/s
x_3	Motor rotor ang. position	rad
x_4	Motor rotor ang. speed	rad/s
	Parameter	**Unit**
α	Inverse of the nozzle moment of inertia	$1/(\text{kg m}^2)$
k_e	Gimbal spring stiffness coefficient	Nm/rad
b_e	Gimbal damping coefficient	Nms/rad
L_a	EMA-to-gimbal point lever arm	m
L_g	MPT transmission ratio	m/rad
k_s	Equivalent structural stiffness coefficient	N/m
η_e	Direct efficiency factor	-
R_m	EM stator equivalent resistance	Ω
L_m	EM stator equivalent inductance	H
k_t	EM torque coefficient	Nm/A
J_m	EM moment of inertia	kg m^2
b_m	EM viscous friction coefficient	Nms/rad

$$
\begin{aligned}
y_1 &= \omega_m = x_4 \\
y_2 &= y_a = L_g x_3 \\
y_3 &= F_e = -L_a k_s x_1 + L_g k_s x_3
\end{aligned} \tag{39}
$$

where states, inputs, outputs and parameters are summarized in Table 6. Note that all the moments of inertia are expressed with respect to point S. In Equation (38), the inputs are the motor torque ($u_1 = C_m$), and the vehicle-induced loads (u_2) introduced hereafter. States x_1 and x_2 express the nozzle rotational dynamics including the inertial effect together with the rotational spring-damper mechanism provided by the gimbal itself; x_3 and x_4 describe the electric motor dynamics.The outputs, y_1 to y_3, correspond respectively to the motor speed (ω_m), stroke position (y_a) and force measurement (F_e).

Note that this model is equivalent to the combination of PDE-L1, EM-L1, MPT-L2 and nozzle load models.

5.1. Computation of the vehicle-induced loads

The vehicle-induced loads affecting the nozzle dynamics are here introduced. The vehicle dynamics can noticeably impact the behavior of the TVC system: the dual reaction effect produced by the nozzle on the whole vehicle dynamics is instead named Tail-Wag-Dog (TWD) effect and its derivation is to be studied separately for modeling, simulation and control design of the rocket. The derivation is performed in three dimensions, but the result is applicable also when considering only a single thrust vectoring direction. Note that in this Section we mean to provide an analytical expression to the vehicle-induced loads from the engine side without detailing the TWD effect at the vehicle side. However, in the simulations considering the whole vehicle of Section 8.2, the interaction between engine/nozzle and vehicle is inherently accounted for by the multibody modeling within the proposed acausal simulation framework.

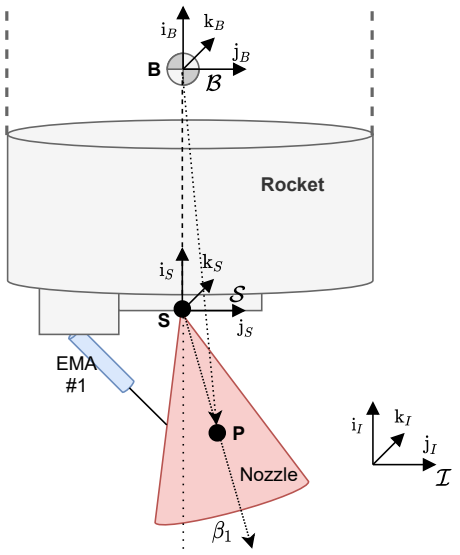

Figure 11: Visualization of the reference frames for vehicle-induced load computation.

Figure 11 depicts the frames of interest: $\mathcal{S}$, defined by $\{S, \mathrm{i}_S, \mathrm{j}_S, \mathrm{k}_S\}$, is the vehicle structural frame, conveniently located at the TVC gimballing point and with the i_S axis pointed to the vehicle's tip; with similar notation, $\mathcal{B}$ is the body frame, a translation of $\mathcal{S}$ to the vehicle's center of mass (point B), while $\mathcal{I}$ represents an inertial frame. To compute the vehicle-induced additional torque acting on the EM, the nozzle acceleration must be firstly derived as:

$$
\begin{aligned}
(\mathbf{a}^P)_{\mathcal{I}} = (\mathbf{a}^B)_{\mathcal{I}} + (\mathbf{a}^P)_{\mathcal{B}} + \boldsymbol{\alpha}_{\mathcal{B}/\mathcal{I}} \times (\mathbf{r}^P)_{\mathcal{B}} \\
+ \underbrace{2\boldsymbol{\omega}_{\mathcal{B}/\mathcal{I}} \times (\mathbf{v}^P)_{\mathcal{B}}}_{\text{Coriolis}} + \underbrace{\boldsymbol{\omega}_{\mathcal{B}/\mathcal{I}} \times (\boldsymbol{\omega}_{\mathcal{B}/\mathcal{I}} \times (\mathbf{r}^P)_{\mathcal{B}})}_{\text{centrifugal}}
\end{aligned} \tag{40}
$$

where the notation $(\mathbf{a}^P)_{\mathcal{I}}$ expresses a vector $\mathbf{a}$ referred to point P with derivative taken with respect to frame $\mathcal{I}$, whereas $\boldsymbol{\alpha}_{\mathcal{B}/\mathcal{I}}$ refers to a vector $\boldsymbol{\alpha}$ referred to frame $\mathcal{B}$ with respect to frame $\mathcal{I}$. The vectorial quantities $\mathbf{a}$, $\mathbf{v}$ and $\mathbf{r}$ denote acceleration, velocity and position vectors, whereas $\boldsymbol{\alpha}$ and $\boldsymbol{\omega}$ are angular acceleration and velocity. Note that vectors in Equation (40) can be conveniently expressed in $\mathcal{B}$ frame. In the following, we assume that $(\mathbf{v}^P)_{\mathcal{B}}$ and $(\mathbf{a}^P)_{\mathcal{B}}$ are small, thus their terms negligible. Point P is placed at the nozzle center of mass. The load force derived from the nozzle acceleration can be expressed as

$$
\mathbf{F_l} = -M_s (\mathbf{a}^P)_{\mathcal{I}}, \tag{41}
$$

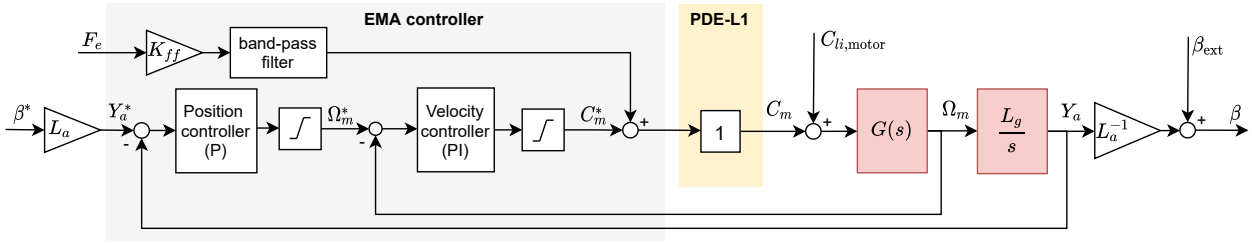

Figure 12: TVC (and EMA) control system architecture. The input $C_{li,\text{motor}}$ is a torque to the motor generated by the vehicle dynamic loads. The input β_{ext} is a generic disturbance at the gimbal point.

where M_s is the nozzle mass. Consequently, the torque at the gimbal point from such a force is:

$$\mathbf{C}_{li,\text{gimbal}} = (\mathbf{r}^P)_S \times \mathbf{F_l}. \tag{42}$$

By performing the necessary substitutions and considering a small angle assumption for the TVC deflections β_1 and β_2, $\mathbf{C}_{li,\text{gimbal}}$ is:

$$\mathbf{C}_{li,\text{gimbal}} = \begin{bmatrix} +\mathbf{F_l}(2)L_e\beta_2 - \mathbf{F_l}(3)L_e\beta_1 \\ -\mathbf{F_l}(1)L_e\beta_2 - \mathbf{F_l}(3)L_e \\ +\mathbf{F_l}(1)L_e\beta_1 + \mathbf{F_l}(2)L_e \end{bmatrix}, \tag{43}$$

where $L_e = \|(\mathbf{r}^P)_S\|$.

By considering the adopted convention, $\mathbf{C}_{li,\text{gimbal}}(3)$ affects EMA #1, the related motor load torque is:

$$C_{li,\text{motor}_1} = \frac{\mathbf{C}_{li,\text{gimbal}}(3)L_g}{L_a\eta_e}. \tag{44}$$

A similar relation holds for EMA #2 after considering $\mathbf{C}_{li,\text{gimbal}}(2)$.

6. The EMA embedded control system

In this Section, the embedded control system is described. Three nested loops are usually employed as a compromise between disturbance rejection and simplicity. One loop drives the current (hence torque), one regulates the motor angular velocity, and the outermost the stroke displacement. Given that the current loop is several orders of magnitude faster than the velocity loop, this can be neglected and considered as an unitary gain function. Therefore, the adopted scheme is represented in Figure 12 .

The synthesis model corresponds to the linear one described in Section 5. The motor viscous friction (with coefficient b_a) is neglected for simplicity. After symbolic manipulation and by applying the Laplace operator, the transfer function from an input torque C_m to the motor angular rate ω_m is:

$$G(s) = \frac{\Omega_m(s)}{C_m(s)} = \frac{J_m^{-1}(s^2 + n_1 s + n_2)s}{s^4 + d_1 s^3 + d_2 s^2 + d_3 s + d_4}, \tag{45}$$

with

$$n_1 = b_e\alpha \tag{46}$$

Table 7
EM and PDE models compatibility.

		EM		
		L1	L2	L3
PDE	L1	✓	×	×
	L2	✓	×	×
	L3	×	✓	✓
	L4	×	✓	✓

$$n_2 = \alpha\left(k_e + L_a^2 k_s\right) \tag{47}$$

$$d_1 = n_1 + b_m J_m^{-1} \tag{48}$$

$$d_2 = n_2 + \left(L_g^2 k_s \eta_e^{-1} + b_m\right) J_m^{-1} \tag{49}$$

$$d_3 = \left(L_g^2 k_s \eta_e^{-1} n_1 + b_m n_2\right) J_m^{-1} \tag{50}$$

$$d_4 = \left(n_2 L_g^2 k_s - \alpha k_s^2 L_g^2 L_a^2\right) \eta_e^{-1} J_m^{-1}. \tag{51}$$

The transfer function to the stroke displacement y_a, following Equation (1), is:

$$G_y(s) = \frac{Y_a(s)}{C_m(s)} = \frac{L_g}{s} G(s). \tag{52}$$

The position and velocity controllers are chosen to be P and PI regulators. The velocity loop includes the integral action for better disturbance rejection. The control gains are tuned using the H_∞ synthesis technique by setting appropriate requirements on the maximum roll-off frequency and the tracking of an ideal closed-loop transfer function [49].

The effect of the spring k_s may sometimes need to be attenuated [35]. If this is the case, a load sensor at the screw-engine connection point can be used. Therefore, a force feedback compensation law to dampen the parasitic oscillations can be included in the control system too. This is normally carried out by applying a band-pass filter with gain K_{ff} to the sensed force which passes only the frequencies to be compensated for, and, after a suitable conditioning, injecting an additional torque to the control command C_m^*.

7. Frequency-domain analysis

In this Section, the proposed models are compared in the frequency domain. This type of analysis is important

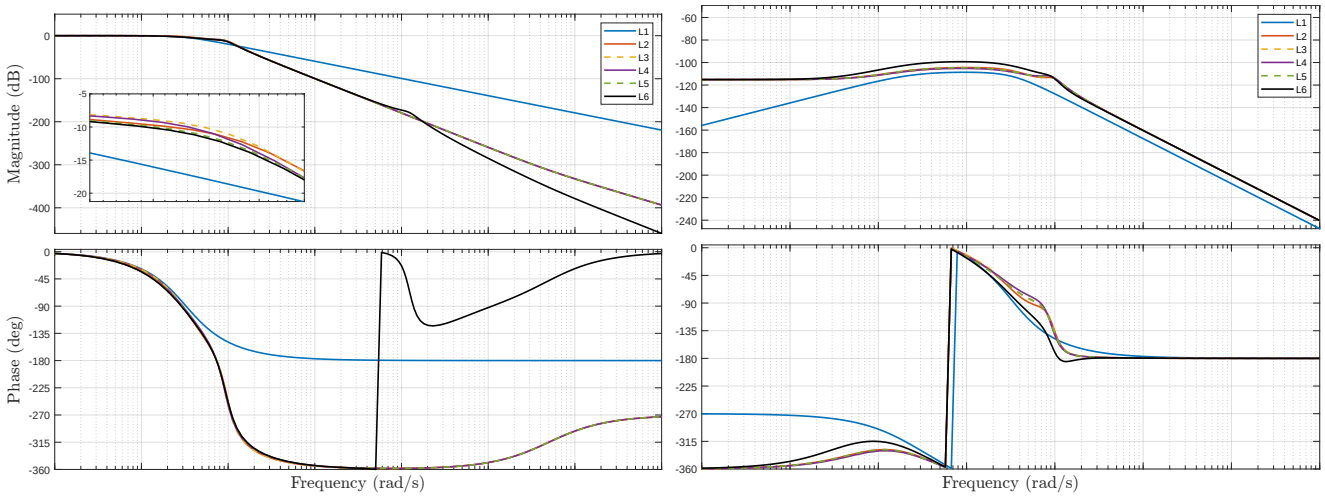

(a) From β^* to β. (b) From β_{ext} to β.

Figure 13: Bode diagrams of the MPT models.

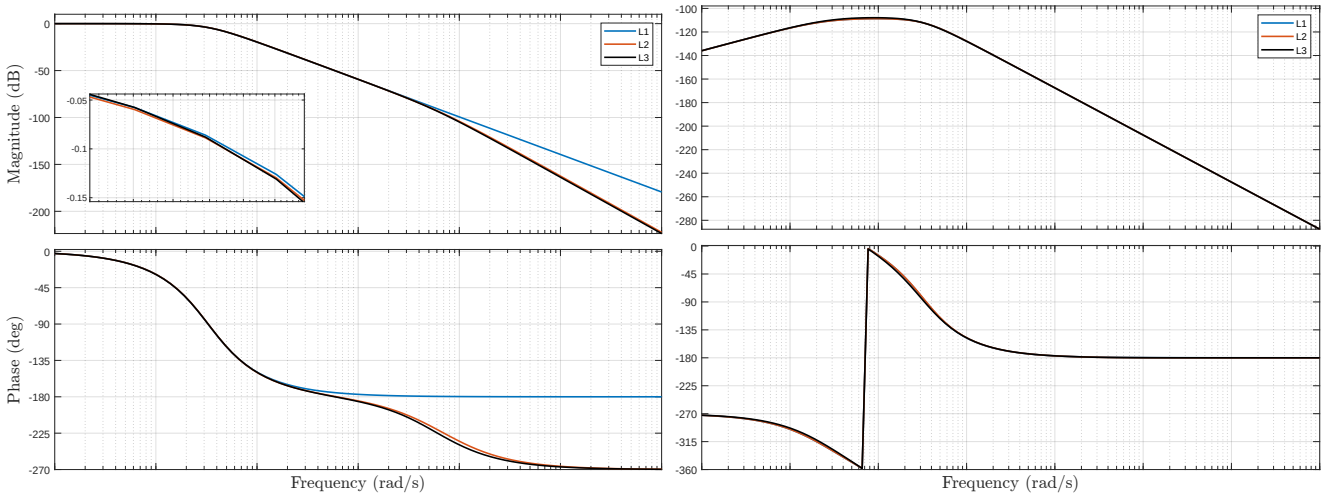

(a) From β^* to β. (b) From β_{ext} to β.

Figure 14: Bode diagrams of the EM models.

because most TVC requirements are specified as gain and phase bounds over frequency.

For all nonlinear models, the linearization is performed numerically by the Dassault Systémes Dymola software (a Modelica-based integrated development environment) on the closed-loop system. The control system is set up as in Section 6. Note that, as detailed in Appendix A, the EM and PDE models can be combined only following Table 7 to comply with the required physical interfaces. The nozzle load is included as rotational inertia together with the gimbal spring-damper mechanism.

7.1. EMA components

The different implementations of the EMA components are hereafter compared. In this Section, only one vectoring axis is considered. The input is the reference TVC angle and the output is the actual TVC angle (from β^* to β). Furthermore, the effect of a generic disturbance torque β_{ext} (Figure 12) acting at a gimbal point is analyzed as well. This disturbance may also represent how the vehicle-induced loads enter in the TVC dynamics.

Figure 13a shows the frequency response of all MPT models. The complementary models are PDE-L1 and EM-L1, so that no unnecessary dynamics is introduced. MPT-L1 linearized model shows a second order dynamics generated by the motor and nozzle inertia, and by the gimbal spring-damper. MPT-L2 adds the presence of a connection spring between the EMA and the nozzle, therefore its Bode plot exhibits a resonance just after the roll-off frequency. MPT models from MPT-L3 to MPT-L5 only differ for the presence of a different type of friction and, given the plot scale, are almost overlapped. In practice, the presence of the friction moves the poles of the overall closed loop to

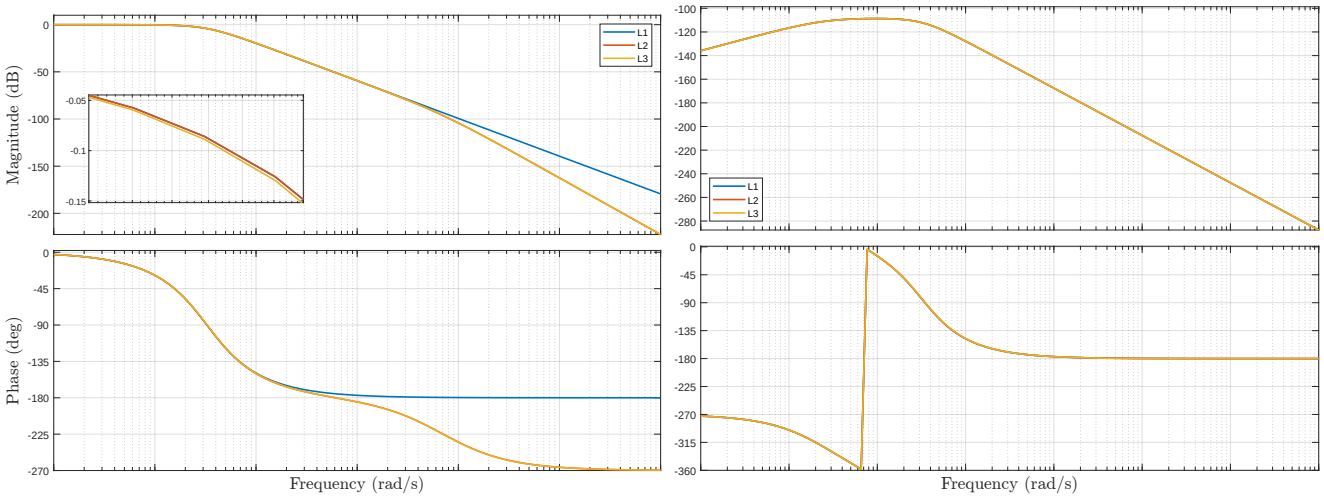

(a) From β^* to β. (b) From β_{ext} to β.

Figure 15: Bode diagrams of the PDE models (L4 is excluded).

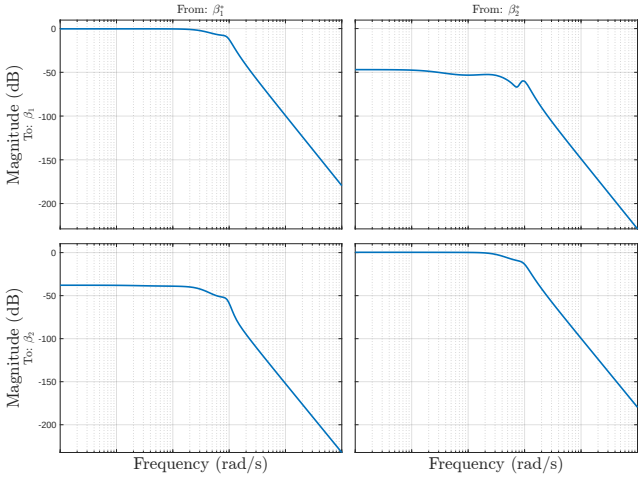

Figure 16: Bode diagrams (magnitude only) highlighting the TVC channels cross-coupling.

a lower frequency and increases the damping action at the resonance. Lastly, the MPT-L6 model introduces the backlash. Linearizing the backlash effect is not possible in a non-contact condition; when contact happens, the related contact spring-damper mechanism introduces its dynamics as well and justifies the second resonance at higher frequency of the MPT-L6 curve. In Figure 13b the disturbance rejection of the TVC closed loop is shown. It can be observed that similar conclusions can be drawn also in this case. Most importantly, MPT-L1 shows a perfect rejection of steady state disturbance torques. This can lead to a wrong EMA control system design if this model is used for synthesis. All other models exhibit an attenuation of the torque at low frequency, therefore constant disturbances cannot be completely filtered out. This behavior is due to the EMA-nozzle spring and to the fact that the position loop is not closed accounting for the TVC angle β (which is not measurable), but the EMA stroke position y_a. MPT-L6 shows an overall worse disturbance rejection due to the presence of backlash.

Figure 14a shows the frequency response when varying the EM models. To complement the EMA composition, PDE-L1 or PDE-L3 (Table 7), and MPT-L1 are used. From EM-L2 is necessary to introduce the current closed-loop as well to be able to input the right voltage to the physical model of the motor. Therefore, EM-L2 and EM-L3 slopes are lower at high frequency. The difference between EM-L2 and EM-L3 lies in the friction and manifests in the same way as the MPT case with a very small bandwidth reduction. Figure 14b evidences that the EM model fidelity does not alter the disturbances rejection properties evidenced before.

Lastly, Figure 15a highlights the impact of the different PDE models. In the plots, L4 is excluded because of the impossibility to accurately linearize the inverter dynamics. It can be seen that PDE-L1 and PDE-L2 have the same frequency dynamics until the current closed loop frequency, where the slope further decreases. PDE-L3 is qualitatively similar to L2. Figure 15b shows that there is no substantial difference in the disturbance rejection between the PDE models.

7.2. TVC system couplings

Hereafter, the whole TVC system is analyzed in the frequency domain. Focus is put on the TVC channels cross-couplings and on the interference of rolling torque at vehicle level to the TVC. The EMA model is used as described in Appendix A.2 to form a three-dimensional TVC model which is then linearized as the in previous Section. For both assessments, the considered EMA models composition is: PDE-L1, EM-L1, MPT-L2, plus the nozzle inertia and gimbal spring-damper.

Figure 16 shows the coupling between the two TVC closed loops in the frequency domain. It can be seen that cross-couplings effects (i.e. off-diagonal channels) are significantly attenuated but are not null. This is due to the

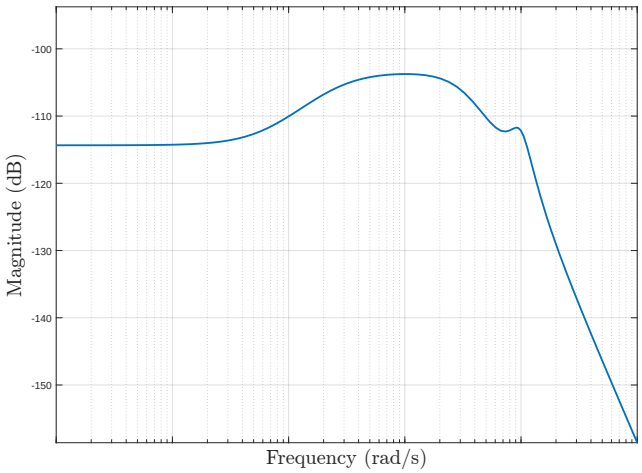

Figure 17: Bode diagram (magnitude only) of the single-channel closed-loop TVC subject to a nozzle rolling torque.

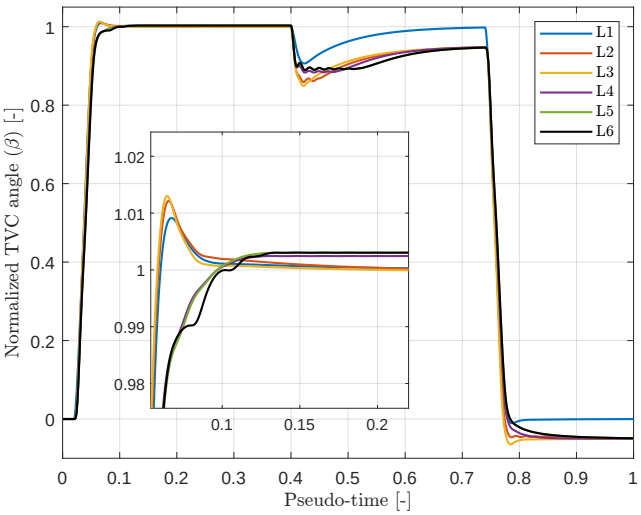

Figure 18: MPT models dynamic response to step inputs and disturbance.

geometrical construction of the system itself and because of the non-negligible rolling moment of inertia of the nozzle.

Figure 17 shows the effect of a nozzle rolling torque in the frequency domain to the TVC closed loop. This effect is relevant because it can lead to a resonant response in the presence of roll perturbations especially the TVC angles are not zero. The Figure shows the case when the TVC model around linearized with $\beta_1 = \beta_2 = 2$ deg and $\dot{\beta}_1 = \dot{\beta}_2 = 0$ deg/s and demonstrates that the vehicle rolling torque can stimulate a control system reaction at EMA level as well.

8. Time-domain analysis

Hereafter, simulation results in the time domain are presented and discussed. In Section 8.1, standalone TVC models (without vehicle dynamics) are simulated to compare the behaviour of the EMA components with incrementally increasing level of fidelity. In this case, there are no vehicle-induced loads acting on the system. In Section 8.2, some TVC model variants are integrated in a full vehicle simulated during its ascent flight. The CALLISTO RLV demonstrator is taken as test case [5, 50].

In both cases, the relevant EMA and TVC parameters are taken from CALLISTO TVC design or obtained, after adequate scaling, from Fu [33]. As such, care must be taken when extrapolating the conclusions from this section to significantly different TVC systems. The time and magnitudes of plots are depicted using normalized units.

8.1. Standalone TVC model

The standalone TVC model consists of interconnected PDE, EM and MPT physical models, plus the nozzle inertia and the gimbal spring-damper mechanism. The adopted control scheme is again the one introduced in Section 6. PDE, EM and MPT are considered separately and the respective simulation model fidelity levels compared and analyzed. The differences between the EMA component models are assessed by looking at the response from a TVC angle command β^* to the actual TVC angle β. For a clearer assessment, no TVC axes cross-couplings are considered now. All simulations are performed with the same TVC angle command profile. At about half the simulation time, an external step-like input torque β_{ext} is injected at the gimballing point and remains active until the end of the simulation. Close to the end of the simulation, another step β^* command resets the angle to zero.

Figure 18 shows the differences between the MPT implementations, where, to complement the simulation model, PDE-L1 and EM-L1 are used. It can be seen that MPT-L1 to MPT-L3 have a similar dynamical behavior with slight differences: they all tend to overshoot the setpoint because of the control architecture choices and, starting from MPT-L2, due the presence of a mechanical compliance which amplifies this effect. Note also that MPT-L1 is the only model able to track the setpoint with zero steady-state error; this is due to the absence of the EMA-to-nozzle spring, as seen in Section 7.1 (Figure 13a). This manifests clearly when an external torque is injected. In MPT-L3, the viscous friction plays a marginal role, in agreement with [28], because it is directly proportional to the stroke velocity, whose setpoint $v_a^* = \omega_m^* L_g$ is generally saturated. Whenever the Coulomb, Stribeck and load-dependent frictions are introduced (MPT-L4 to MPT-L6), the force opposing the motion increases and the overshoot reduces. Moreover, the presence of the Coulomb friction causes y_a to never reach zero steady-state error, because, while overshooting and the velocity nulls before changing sign, the control action might simply not be enough to counteract the Coulomb friction again and precisely drive the actuator to the required setpoint. This verifies also because no extra integral action is included in the position loop. MPT-L5 shows that the load-dependent friction can also slightly alter the closed-loop response. However, its relevance is less obvious when only one regime is explored, that is with the EMA driving and the nozzle acting as "opposing" load. This aspect will be deepened in future works. In MPT-L6, the response is slightly delayed as

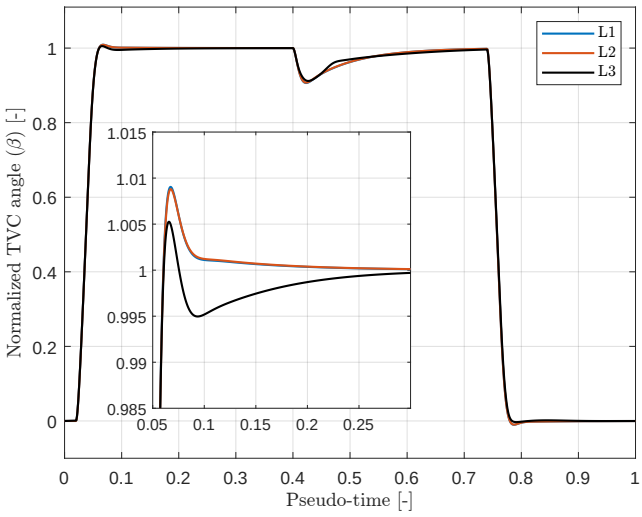

Figure 19: EM model responses to step inputs and external disturbance.

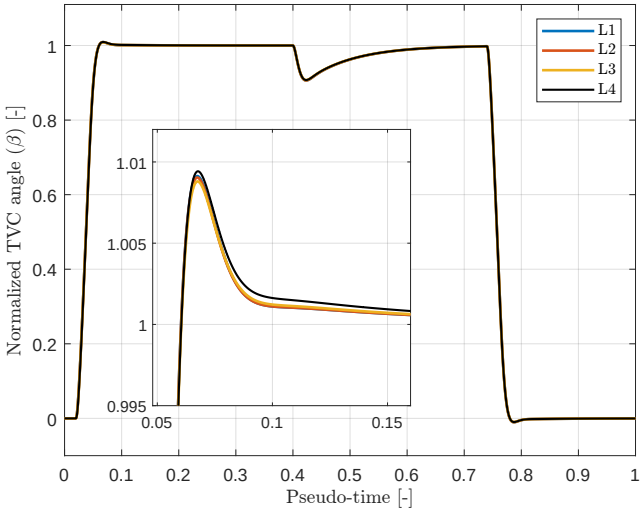

Figure 20: PDE dynamic responses to step inputs and disturbance.

a consequence of the presence of backlash; the lost motion is clearly evidenced close to the setpoint where the motor torque decreases. In this situation, the preload spring effect is visible and causes a mild wobbling before mechanical contact is re-established.

Figure 19 displays the difference between the EM models. Complementary models are MPT-L1, and PDE-L1 or PDE-L3 (Table 7). The figure evidences that shifting the EM modeling efforts into the electrical (EM-L1 to EM-L2) domain delivers little differences to the overall dynamics. Of more impact is, instead, the presence of the dissipative losses (in EM-L3) that increase the response delay, in accordance to what seen in Section 7.1. Observing the closed loop at TVC deflection angle level evidences how the cogging torque and hysteresis effects are completely masked.

Figure 20 shows the dynamic differences introduced by the different PDE models. Here, EM-L1 or EM-L2 (Table 7), together with MPT-L1. As expected, PDE-L2 introduces a

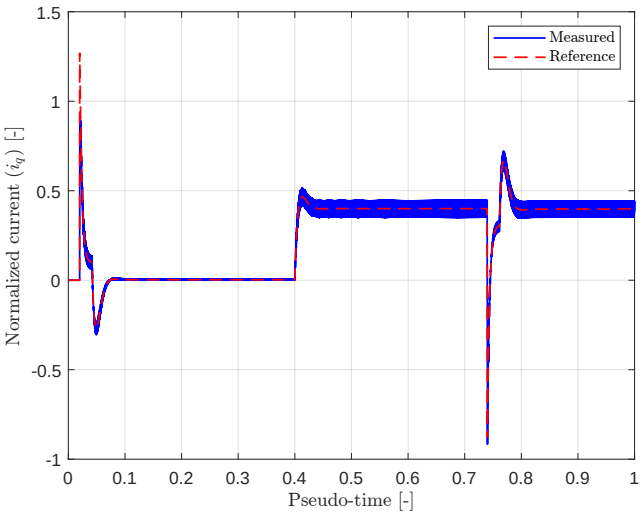

Figure 21: Quadrature current tracking in PDE-L4 model.

small delay in the response; nevertheless, all responses up to PDE-L4 do not differ significantly. The PDE-L4 introduces the inverter dynamics; Figure 21 shows the quadrature current tracking performance; i_q is obtained after a Park transformation from the (modulated) three-phase currents outputted by PDE-L4. In view of the above, PDE-L4 adoption is not justified for simulating a TVC system. Due to the high switching frequency (sometimes higher than 10 kHz), PDE-L4 adds a big computational burden and significantly increases the required simulation time. On a consumer PC featuring an Intel® Core™ i5-6300U and within the Dymola environment, simulating PDE-L4 takes about 1200 times longer than PDE-L3. Aside from making the simulation problem numerically stiff, the main cause of the simulation slowness is the huge number of state events caused by state variables chattering (transistor gates opening/closing). Furthermore, it is evident that the PDE is the component that affects the least the overall dynamics; as such, PDE-L2 or PDE-L3 can be mainly considered for an effective GNC V&V and for Monte-Carlo simulation campaigns.

As a final comparison, Figure 22 depicts the difference between the lowest-fidelity model (PDE-L1, EM-L1 and MPT-L1), and the highest-fidelity model (PDE-L4, EM-L3 and MPT-L6). By comparing it with the previous component-specific plots, it is confirmed that the different dynamical behavior of the higher-fidelity TVC model with respect to the lowest-one can be mainly attributed to the EMA mechanical power transmission stage. Lastly, attention has to be put at control design stage to which model is employed for synthesis.

8.2. Launch vehicle ascent scenario

For the CALLISTO reusable launch vehicle simulation, four scenarios, summarized in Table 8, are considered. The CALLISTO framework is based on Simulink, therefore the TVC models developed using Modelica have to be first exported as described in Section 2. Its TVC architecture features two orthogonal EMAs [50].

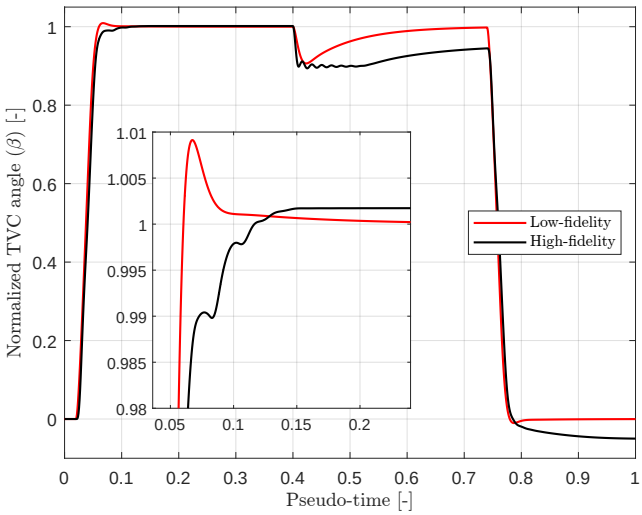

Figure 22: Lowest- and highest-fidelity models (MPT, EM, PDE) dynamic response to step inputs and disturbance.

Table 8
Summary of the scenarios included in the launch vehicle ascent simulations.

Scenario	Full vehicle model	TVC model
#1	Rigid body	Linear
#2	Multibody	MPT-L2
#3	Multibody	MPT-L5
#4	Multibody	MPT-L6

Scenario #1 is purely Simulink-based: equations of motion are of a 6-DoF rigid body referenced to frame $\mathcal{B}$, like in [51]. Actuator forces and torques are then expressed with respect to the latter frame. The TVC system is modeled as described in Section 5, while the vehicle-induced loads computed as in Section 5.1 and injected as an external torque acting on the electric motor. Note that in this case the TVC vectoring directions are not coupled.

Scenarios #2 to #4 include a full vehicle model developed in Modelica. This allows a three-dimensional configuration and cross-coupled dynamics. As already mentioned, the vehicle-induced dynamics acting on the nozzle and the TWD effect (being in practice the action-reaction forces and torques between upper vehicle and nozzle) are inherently accounted for because of the multibody formulation, as deepened in Appendix A. In turn, this also highlights the advantage of using acausal modeling techniques. The whole TVC system model is integrated with a rigid body capturing the dry mass inertial dynamics, and four rigid bodies capturing the propellant static masses. Sloshing and other effects can eventually be included, by modifying this base configuration. Given the results of the previous section, only the effects of different MPT implementations are considered, while EM and PDE models are both L1. Scenario #2 differs from #1 because it effectively shows the consequences when shifting to the aforementioned multibody setting. Scenario #3 evidences the effect of friction, whereas Scenario #4 the backlash effect.

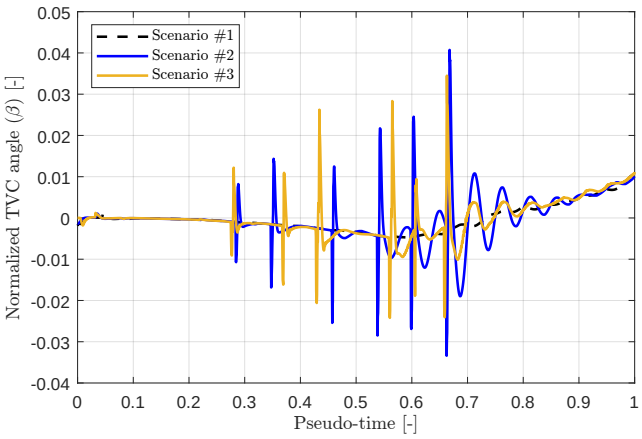

Figure 23: CALLISTO TVC angle (pitching plane) during ascent using Scenarios #1 to #3.

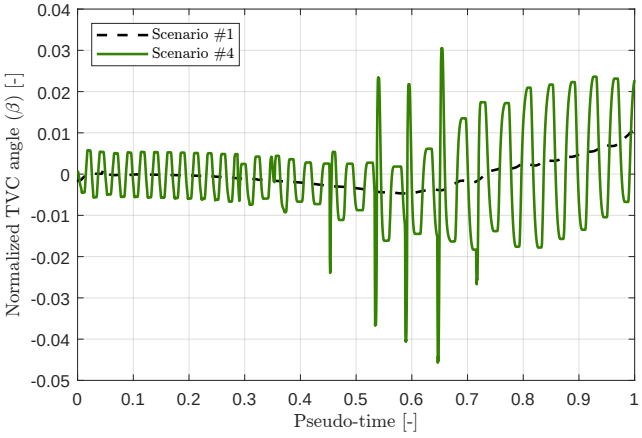

Figure 24: CALLISTO TVC angle (pitching plane) during ascent using Scenarios #1 and #4.

Figure 23 shows the nozzle deflection angle (pitching plane) during the ascent phase. Scenarios #2 and #3 exhibit some spikes and a more oscillatory behavior than the linear model (Scenario #1). This is explained considering that the vehicle rolling motion is controlled by means of an Reaction Control System (RCS) with pulsing thrusters which, in turn, requires the TVC system to also adjust the orientation. This pulsing is then a coupling effect between the RCS and the two TVC actuators, in agreement with Section 7.2.

Scenario #3 exhibits a more damped response as a consequence of the friction effect.

Figure 24 highlights how backlash modifies the TVC behavior. Comparing this figure with Figure 23, it is clear that the backlash-induced mechanical lost motion acts as a dead-zone to the roll disturbances and the overall closed-loop becomes less sensitive to the the RCS pulsing.

9. Conclusions

This paper presented an approach for the physical modeling and simulation of an EMA-based TVC system. The issues regarding this type of modeling have been explained and discussed. The lack of a formal methodology to implement simulation models of the TVC system featuring modularity, minimalism, integrability with other GNC environments, and incremental fidelity, have been addressed. This was possible by adopting a specific modeling strategy enabled by the Modelica modeling language.

The different components of EMAs (power drive, electric motor and mechanical transmission) have been introduced and several models with increasing fidelity levels proposed. The difference between all implementations have been consequently described, and converged in the implementation of a Modelica library for the EMA components and the whole TVC system. While the mechanical EMA components have been implemented considering one dimension (rotational/translational), special Modelica models have been developed to enable their use in three-dimensions for the integration within multibody models. This in turns allows the integration with any launch vehicle model.

In view of this choice, several analyses could be conducted, either in the frequency domain or in the time domain, and both in the one-dimensional and in the three-dimensional cases. The frequency-domain analysis showed that the most impacting component for the assessment of the TVC deflection angle closed loop is the mechanical transmission. The impact of the structural compliance, of the friction effects and the backlash have been highlighted.

The main outcome is that special care is needed when performing the assessment of the onboard software with low-fidelity TVC models. Furthermore, from the disturbance rejection perspective, employing the simplest mechanical transmission model can lead to too optimistic conclusions. This can also be relevant during the control design process and when formulating and analyzing the TVC specifications. On the other hand, the motor model influences the dynamics in a minor manner; instead, the impact of the power electronics to the TVC closed-loop dynamics can be considered negligible. These results have been also confirmed in a time-domain analysis by checking the system closed-loop step response, also in presence of an external disturbance. In the configuration featuring the whole launch vehicle, it was shown how the multibody model is able to clearly exhibit the cross-couplings happening between the two EMAs with the nozzle load and the vehicle dynamics itself.

In future works, the results of this paper will be expanded in the following directions: (1) the TVC/EMA models will be further extended. In particular, the modeling of the EMA elasticity will be taken into account, as well as the stiffness between the EMA and the vehicle anchorage point; (2) the modeling and inclusion of the sensor dynamics will be performed as they can negatively impact the TVC closed-loop dynamics; (3) the impact of higher-fidelity models on the rocket dynamics at descent and landing phases will be studied. This means analyzing in detail the TWD effect in the final mission phases when the propellant is almost exhausted and the engine mass becomes a relevant portion of the overall mass. Moreover, the propellant sloshing, the vehicle flexibility and the nozzle flexibility couplings require also to be explored. Since the proposed framework allows to also scale up the overall vehicle simulation model accuracy without relying on less-representative superposition methods, this aspect will be considered as relevant matter of investigation.

A. Modelica implementation

The TVC and EMA model implementations using Modelica are now described. They have been integrated within the Vertical Landing Vehicles Library (VLVLib), a Modelica package specialized in modeling Vertical Take-off Vertical Landing (VTVL) vehicles [7]. The models discussed in this paper have been integrated by extensively employing the MSL and are included into two different sub-packages: one containing the EMA component dynamics, its embedded controller, testing functions and some assemblies, and a second sub-package that includes the models for the eventual integration with the vehicle dynamics. The architecture is explained in Figure 25. All EMA components and relevant assemblies are contained in sub-packages included within `Actuators.TVC.Components`; internally, the dedicated sub-package `EMA` includes MPT, EM, PDE and the controller models. In launchers, the power electronics and the ACC are normally installed in a physically separated manner from the EMAs and the nozzle. As such, the model `EngineBay` inside the `Assemblies` sub-package instantiates the control system and the required (replaceable) PDE models; here, the nozzle deflection angle command is converted into a stroke displacement setpoint y_a^*. The `EmaBody` model, instead, includes the EM and MPT, as the actual mechanical parts involved in the nozzle actuation. In the same `Assemblies` package, the model `EmaMultibody` transforms `EmaBody` into a 3D TVC model; it means that the uni-dimensional Modelica connectors for the EM and MPT, called *flanges*, are expanded into other types of connectors, called *frames*, for three-dimensional dynamics. This enables in turn its integration within a multibody launcher model.

The integration of the EMA into a full TVC system is performed in the VLVLib sub-package `Parts.TvcEngineSystem`: here, a standalone uni-dimensional TVC model can be created by integrating the `EngineBay` and `EmaBody` models together with a nozzle load (plus gimbal spring-damper). The 3D TVC system is instead composed using `EngineBay`, `EmaMultibody` and a 3D nozzle model; the latter is included as a rigid body. The final TVC multibody model, further explained in Appendix A.2, can then be used to complement the launch vehicle models included in the VLVLib.

A.1. EMA components

The full implementation of the EMA models relies on models spread in different sub-packages, concisely shown in Figure 26. PDE, EM and MPT are modeled starting

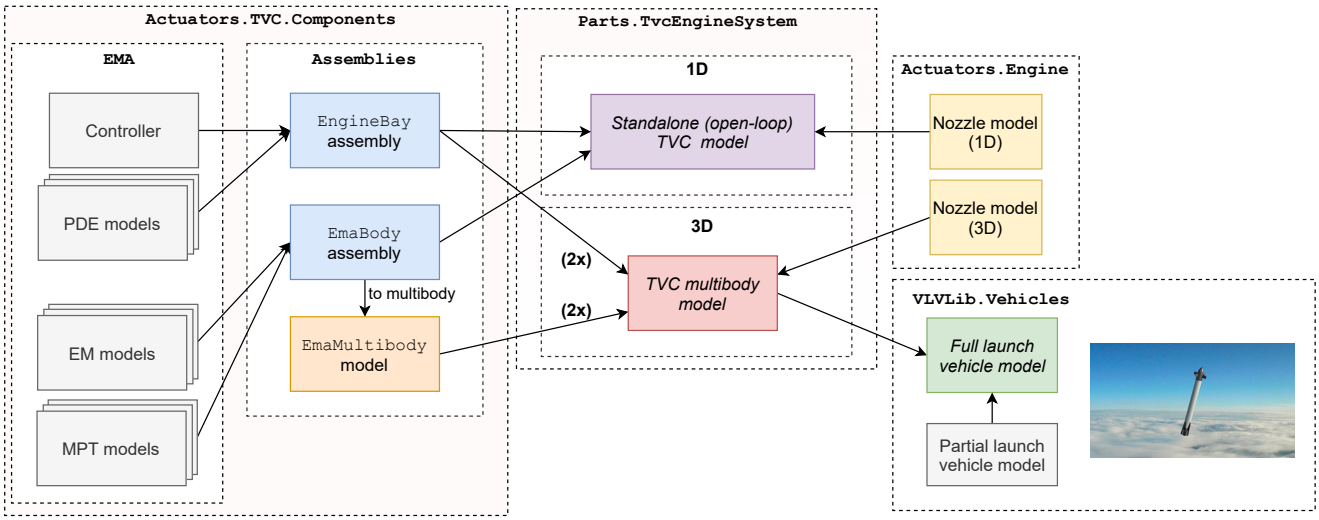

Figure 25: Diagram of the packages architecture to obtain the final standalone TVC system 1D simulation model (in purple) or the 3D one (in red) to be integrated within the whole vehicle dynamics.

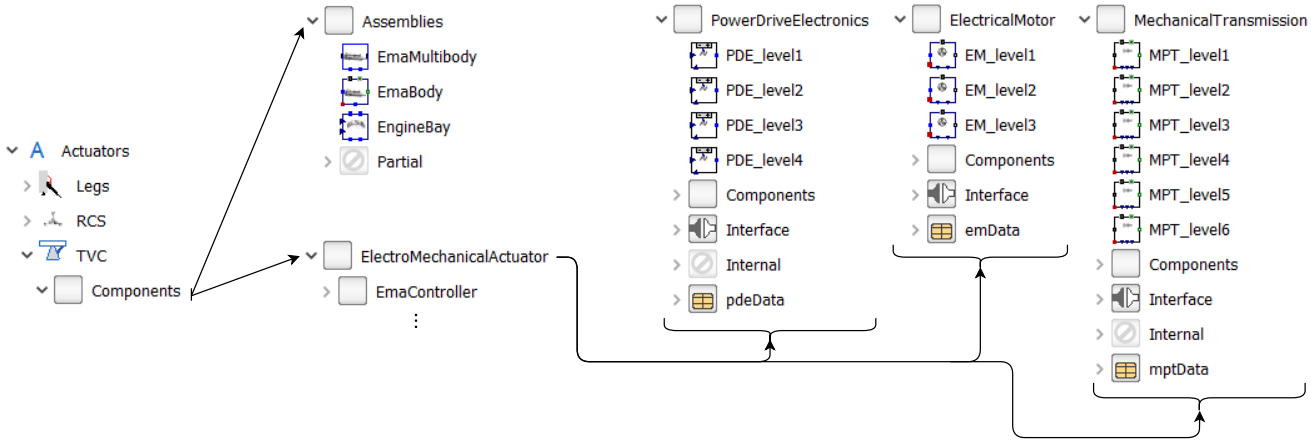

Figure 26: Breakdown of the `VLVLib.Actuators.TVC` package where the EMA components are contained.

with a *partial model*[6] instantiating the interfaces and the components that do not change their implementation over the different levels L[1-*n*]. The specialized models are required to inherit it to guarantee common interfaces and consequently use the Modelica redeclaration feature.

Despite this property, not all models can be arbitrarily combined with each other; this is the case of the electric motor and the power electronics when electrical connectors from `Modelica.Electrical` library are used (Table 7).

One of the biggest difficulties when composing the controller, the PDE, EM and MPT models is the initialization of their state variables. It must be chosen if the load (nozzle) states are to be initialized and therefore the EMA states obtained via a "back-propagation" performed by the Modelica translation engine at compilation time, or the EM/MPT states are initialized, thus deriving the initial nozzle states.

[6] A model that cannot be instantiated alone, but must be necessarily extended.

Furthermore, as the fidelity level of the components increases, new components are to be added and their initialization must be dealt with accordingly.

A.1.1. MPT models implementation

Figure 5 explains the MPT constitutive sub-models and how they are connected. Despite operating within an acausal modeling environment, the components connection order also plays a significant role when determining the simulation results; what is shown is a compromise between mechanical fidelity and letting the MPT model be well-posed for simulation. To enable the EMA to exert reaction forces and torques at its anchorage points, as well as to couple the effects of the whole vehicle, all MPT models include `Support` ports (for both translational and rotational domains). The ideal nut-screw and spring are modeled using the `Rotational.IdealGearR2T` and `TranslationalSpring` models included in the MSL `Mechanics` MSL package. The basic efficiency model is derived from the `LossyGear` MSL component, but modified

to operate in the translational domain, rather than rotational. It is included only in MPT-L1 and MPT-L2, since from MPT-L3 on the mechanical inefficiencies are modeled with friction. The screw mass is present only starting from MPT-L2 on and modeled using `Mechanics.Translational.Components.Mass`. The basic friction (Coulomb, viscous and Strickbeck) is instead modeled via the class `Mechanics.Translational.Components.SupportFriction`. The backlash model is obtained in the translational domain from the MSL's equivalent in the rotational domain; the option of enabling the preload spring as in Equation (13) is included. The implementation of a conservative load-dependent friction model required reworking the MSL `LossyGear` model, as explained in Appendix B.

It is important to notice that numerical problems may arise when compiling and initializing and EMA model with MPT-L6, *i.e.* with backlash effect included. In this case, the combination of the backlash spring and the structural compliance may result in a numerically unsolvable problem. This issue is counteracted by moving the screw mass *after* the backlash component.

A.1.2. EM models implementation

The EM model outputs a rotational displacement and torque via the appropriate Modelica rotational mechanical connector. The EM-L1 model receives as input a torque from the PDE and applies it to a rotational inertia representing the motor rotor. Also in this case, as shown in Figure 6, mechanical supports are included. The EM-L2 model instead employs the full PMSM dynamics, reproduced via the MSL component included in `Electrical.Machines.BasicMachines.SynchronousMachines.SM_PermanentMagnet`. The latter model already includes the possibility of adding some losses; therefore, the EM-L3 model is obtained by suitably extending and modifying EM-L2. The cogging and hysteresis disturbances are instead injected as external torques and modeled separately.

A.1.3. PDE models implementation

The PDE-L1 is a torque command signal C_m^* passthrough, while PDE-L2 contains a PI regulator with saturation and anti wind-up action. The current dynamics is the one explained in Section 4.3.2 and included as a transfer function. PDE-L3 implements a direct-quadrature current controller, therefore a Park transformation is required and, as such, also the mechanical motor rotor angle, provided as input. The transformation is carried out using the models `fromDQ` and `toDQ` contained in `Electrical.Machines.Utilities`. The 3-phase controller voltage output then feeds an ideal voltage source. The PDE-L4 model includes the inverter dynamics; the controller output voltage is first converted into a space phasor and fed into an instantiation of `Electrical.PowerConverters.DCAC.Control.PWM` that generates the boolean signals to feed the inverter gates. The inverter model is taken from `Electrical.PowerConverters.DCAC.Polyphase2Level`.

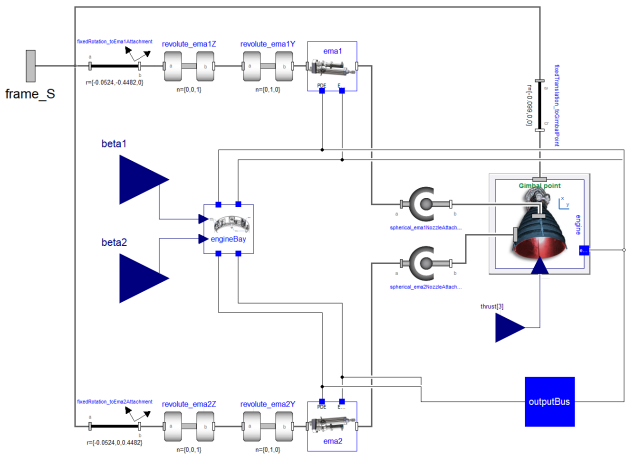

Figure 27: Multibody TVC model diagram view.

A.2. Modeling of the whole TVC system

The full TVC/nozzle assembly is integrated into the `VLVLib.Parts.TvcEngineSystem` package. The sub-package `Architectures` contains the 1D implementation and the full 3D one, whereas the sub-package `Variants` includes models that extend them and redeclare the inner MPT, EM and PDE components according to the specific required combinations. The code in Figure 28 highlights how the models have been redeclared to MPT-L1, EM-L1 and PDE-L2, whereas its diagram view is visible in Figure 27. It can be noticed that the interfaces are the commanded deflection angles and the `frame_S` (corresponding to frame $\mathcal{S}$ - Figure 11) connector that enables the TVC assembly to be connected with the frame $\mathcal{S}$. Furthermore, it can be seen that the nozzle (model `Engine_v1`) is connected to the EMA via a spherical joint. The EMA itself is connected to the vehicle bottom skirt via a universal joint (two rotational joints in series). As introduced in Section 5, the nozzle dynamics is subject to a rotational spring-damper system at the gimbal point.

B. Load-dependent friction model

Capturing Equations (11) and (12) into suitable Modelica models is not an easy task, as including it with the sign(·) operator may induce state variables chattering leading to excessively slow or disrupted simulations. Given that the friction models can be made arbitrarily complex, it is useful to generalize them by capturing the friction force dependence with respect to the speed and direct/indirect efficiency factors. This approach is followed within the mechanical-domain models of the Modelica Standard Library (MSL), where two types of friction models are present within the `Rotational` and `Translational` sub-packages. As of the latest MSL update (version 4.0.0, [44]), they are:

1. `Components.BearingFriction` in the rotational and `Components.SupportFriction` in the translational domain, both handling the velocity-dependent friction;

```
model TvcSystem_v1
    extends VLVLib.Parts.TvcEngineSystem.Architecture.TvcArchitecture(
    ema1(emaBody(
            redeclare TVC.Components.ElectroMechanicalActuator.ElectricalMotor.EM_L1 motor,
            redeclare TVC.Components.ElectroMechanicalActuator.MechanicalTransmission.MPT_L2 mpt)),
    ema2(emaBody(
            redeclare TVC.Components.ElectroMechanicalActuator.ElectricalMotor.EM_L1 motor,
            redeclare TVC.Components.ElectroMechanicalActuator.MechanicalTransmission.MPT_L2 mpt)),
    engineBay(
        redeclare TVC.Components.ElectroMechanicalActuator.PowerDriveElectronics.PDE_L2 pde1,
        redeclare TVC.Components.ElectroMechanicalActuator.PowerDriveElectronics.PDE_L2 pde2),
    redeclare VLVLib.Actuators.Engine.Engine_3D engine,
    spherical_ema1NozzleAttachment(w_rel_a_fixed=false, z_rel_a_fixed=false),
    spherical_ema2NozzleAttachment(w_rel_a_fixed=false));
end TvcSystem_v1;
```

Figure 28: The `TvcSystem_v1` class code. The class inherits the general TVC system architecture and redeclares the EMA components contained in `emaBody` and `engineBay` models as per required fidelity level.

Table 9
MSL's `LossyGear` implementation of the friction.

ω_A	τ_A	$\Delta\tau =$
> 0	≥ 0	$(1-\eta_{mf1})\tau_A + \lvert\tau_{bf1}\rvert$
> 0	< 0	$(1-1/\eta_{mf2})\tau_A + \lvert\tau_{bf2}\rvert$
< 0	≥ 0	$(1-1/\eta_{mf2})\tau_A - \lvert\tau_{bf2}\rvert$
< 0	< 0	$(1-\eta_{mf1})\tau_A - \lvert\tau_{bf1}\rvert$

Table 10
`GeneralTranslFriction` modified implementation of the friction.

ω_A	τ_A	$\Delta\tau =$
> 0	≥ 0	$(1/\eta_{mf1}-1)F_B + \lvert f_{bf1}\rvert/\eta_{bf1}$
> 0	< 0	$(\eta_{mf2}-1)F_B + \lvert f_{bf2}\rvert\eta_{mf2}$
< 0	≥ 0	$(\eta_{mf2}-1)F_B - \lvert f_{bf2}\rvert\eta_{mf2}$
< 0	< 0	$(1/\eta_{mf1}-1)F_B - \lvert f_{bf1}\rvert/\eta_{bf1}$

2. `Components.LossyGear` (only in the `Rotational` subpackage) also accounting for the mesh efficiency. It refers to the additional friction caused by the load-induced increased mechanical contact.

Both cases are explained in detail in [52].

To implement Equation (12), the `LossyGear` model is taken as reference and is not derived again here (the reader can refer to [52], Section 2). What must be recalled is that the flanges torque balance can be rewritten by collecting bearing and mesh friction into a term $\Delta\tau$ as:

$$\tau_B = -\tau_A + \Delta\tau, \tag{53}$$

where subscripts $\cdot_A$ and $\cdot_B$ indicate the friction mechanical model connection flanges. The term $\Delta\tau$ depends on the direct and inverse mesh friction coefficient η_{mf1} and η_{mf2}, and on the direct and inverse bearing frictions τ_{bf1} and τ_{bf2}. This is reported in Table 9 where each row can be referred to as a single 'power quadrant'.

For the EMA case, a variant of `LossyGear` is firstly created in the translational domain as well. Therefore we refer hereafter to friction forces rather than torques. In [31], Maré analyzes the difficulties and the choices to be made when implementing friction models with load-dependent contributions. They are resumed below:

1. the decomposition order, that is whether the load-independent (LI) friction is considered before or after the load-independent part;
2. which force is used to compute the power quadrant (F_A or F_B, translational equivalents of τ_A and τ_B);
3. which force is used to compute the load-dependent friction, *i.e.*, recalling Equation (12), if $F_L = F_A$ or $F_L = F_B$.

The work in [31] shows that these choice significantly impact the dynamic behavior of the final mechanical system. In order to respect specific EMA requirements (also of interest for launch vehicles), [31] concludes that: (1) the LI friction has to be computed first; (2) there is the need to introduce another region, called 'transition' region, to avoid specific problems with the power quadrant switching; (3) the force at the load side F_B is to be used to compute $\Delta\tau$.

For these reasons, a new Modelica model called `GeneralTranslFriction` is implemented including those outcomes. The friction computation is modified as in Table 10. This in general provides more conservative (higher friction) and consistent results in all dynamic regimes. The transition region is instead introduced as expressed with respect to the force to the load F_B as in the Table 6 of [31]. For conciseness reasons, further implementation details, as well as an analysis on the impact to a launch vehicle TVC model, will be given in future works.

Declaration of competing interest

The authors declare that they have no competing interests.

Funding sources

This work is funded by the European Space Agency (ESA) under PhD grant nr. 4000134582/21/NL/GLC and the German Aerospace Center (DLR).

References

[1] L. Hoffman, M. Baker, S. Glynn, M. Darley, P. Beck, Reusable Electron: Analysis of Progress Toward the World's First Reusable Commercial Small Rocket, in: Small Satellite Conference, Logan (Utah), USA, 2022, p. 7.

[2] P. Baiocco, Overview of reusable space systems with a look to technology aspects, Acta Astronautica 189 (2021) 10–25.

[3] H. W. Jones, The Recent Large Reduction in Space Launch Cost, in: International Conference on Environmental Systems, Albuquerque (NM), USA, 2018.

[4] A. Marwege, J. Klevanski, J. Riehmer, D. Kirchheck, S. Karl, D. Bonetti, J. Vos, M. Jevons, A. Krammer, J. Carvalho, Retro Propulsion Assisted Landing Technologies (RETALT): Current Status and Outlook of the EU Funded Project on Reusable Launch Vehicles, in: 70th International Astronautical Congress (IAC), Washington D.C., USA, 2019.

[5] E. Dumont, M. Illig, S. Ishimoto, C. Chavagnac, Y. Saito, S. Krummen, S. Eichel, H. Martens, S. Giagkozoglou, J. S. Häseker, T. Ecker, J. Klevanski, F. Krziwanie, W. Rotärmel, S. Schröder, A. Schneider, C. Grimm, S. Woicke, M. Sagliano, M. Schlotterer, M. Markgraf, B. Braun, M. Aicher, L. E. Briese, I. Petkov, J. Riehmer, B. Reimann, CALLISTO: A Prototype Paving the Way for Reusable Launch Vehicles in Europe and Japan, in: 73rd International Astronautical Congress (IAC), Paris, France, 2022. URL: https://elib.dlr.de/188663/.

[6] S. Farì, D. Seelbinder, S. Theil, Advanced GNC-oriented modeling and simulation of Vertical Landing vehicles with fuel slosh dynamics, Acta Astronautica 204 (2022) 294–306.

[7] S. Farì, The Vertical Landing Vehicles Library (VLVLib): A Modelica-based approach to high-fidelity simulation and verification of GNC systems for reusable rockets, in: 73rd International Astronautical Congress (IAC), Paris, France, 2022. URL: https://elib.dlr.de/188514/.

[8] E. Balaban, J. J. Alonso, An Approach to Prognostic Decision Making in the Aerospace Domain, volume 4 of *1*, Annual Conference of the PHM Society, 2012. doi:10.36001/phmconf.2012.v4i1.2098.

[9] K. Kawatsu, S. Tsutsumi, M. Hirabayashi, D. Sato, Model-based fault diagnostics in an electromechanical actuator of reusable liquid rocket engine, in: AIAA Scitech 2020 Forum, American Institute of Aeronautics and Astronautics, Orlando, FL, 2020. doi:10.2514/6.2020-1624.

[10] N. Paulino, C. R. Arroyos, L. Ferreira, M. Pascucci, P. Cachim, P. Lourenço, J. A. García, D. Navarro-Tapia, A. Marcos, M. Lalami, P. Alexandre, P. Simplicio, S. Bennani, M. Casasco, Fault Tolerant Control for a Cluster of Rocket Engines – Methods and outcomes for guidance and control recovery strategies in launchers, in: ESA GNC-ICATT, Sopot, Poland, 2023.

[11] B. Bjelde, P. Capozzoli, G. Shotwell, The SpaceX Falcon 1 Launch Vehicle Flight 3 Results, Future Developments, and Falcon 9, in: Proceedings of the International Astronautical Congress, Glasgow, Scotland, 2008. URL: http://iacse.commercial-space.net/wp-content/uploads/2008/10/iac-08d213.pdf.

[12] Rocket Lab, Launch - Payload Users Guide 6.5, 2020. URL: https://www.rocketlabusa.com/assets/Uploads/Rocket-Lab-Launch-Payload-Users-Guide-6.5.pdf.

[13] J.-C. Maré, J. Fu, Review on signal-by-wire and power-by-wire actuation for more electric aircraft, Chinese Journal of Aeronautics 30 (2017) 857–870.

[14] A. Garcia, I. Cusido, J. Rosero, J. Ortega, L. Romeral, Reliable electro-mechanical actuators in aircraft, IEEE Aerospace and Electronic Systems Magazine 23 (2008) 19–25.

[15] G. Qiao, G. Liu, Z. Shi, Y. Wang, S. Ma, T. C. Lim, A review of electromechanical actuators for More/All Electric aircraft systems, Proceedings of the Institution of Mechanical Engineers, Part C: Journal of Mechanical Engineering Science 232 (2018) 4128–4151.

[16] L. B. Bates, D. T. Young, Developmental Testing of Electric Thrust Vector Control Systems for Manned Launch Vehicle Applications, in: 41st Aerospace Mechanisms Symposium, Pasadena, CA, 2012. URL: https://ntrs.nasa.gov/citations/20120014541.

[17] C. Carnevale, P. Resta, Vega Electromechanical Thrust Vector Control Development, in: 43rd AIAA/ASME/SAE/ASEE Joint Propulsion Conference Exhibit, American Institute of Aeronautics and Astronautics, Cincinnati, OH, 2007. doi:10.2514/6.2007-5812.

[18] T. Vanthuyne, An electrical thrust vector control system for the VEGA launcher, in: 13th European Space Mechanisms and Tribology Symposium, Vienna, Austria, 2009.

[19] G. Dee, T. Vanthuyne, A. Potini, I. Pardos, G. De Crombrugghe, Electromechanical thrust vector control systems for the VEGA-C launcher, in: 8th European Conference For Aeronautics And Space Sciences (EUCASS), Madrid, Spain, 2019. doi:10.13009/EUCASS2019-186.

[20] E. Balaban, P. Bansal, P. Stoelting, A. Saxena, K. F. Goebel, S. Curran, A diagnostic approach for electro-mechanical actuators in aerospace systems, in: 2009 IEEE Aerospace Conference, IEEE, Big Sky, MT, USA, 2009, pp. 1–13. doi:10.1109/AERO.2009.4839661.

[21] M. D. L. Dalla Vedova, A. Germanà, P. C. Berri, P. Maggiore, Model-Based Fault Detection and Identification for Prognostics of Electromechanical Actuators Using Genetic Algorithms, Aerospace 6 (2019) 94.

[22] J. W. Bennett, Fault Tolerant Electromechanical Actuators for Aircraft, Ph.D. thesis, Newcastle University, 2010.

[23] D. Ossmann, F. L. J. van der Linden, Advanced sensor fault detection and isolation for electro-mechanical flight actuators, in: 2015 NASA/ESA Conference on Adaptive Hardware and Systems (AHS), IEEE, Montreal (QC), Canada, 2015, pp. 1–8. doi:10.1109/AHS.2015.7231162.

[24] S. Farì, D. Seelbinder, S. Theil, P. Simplicio, S. Bennani, Sensor fault detection and isolation for electro-mechanical actuators in a reusable launch vehicle TVC system, in: 10th European Conference For Aeronautics And Space Sciences (EUCASS), Lausanne, Switzerland, 2023. doi:10.13009/EUCASS2023-504.

[25] T. M. Barrows, J. S. Orr, Engine interactions, in: Dynamics and Simulation of Flexible Rockets, Elsevier, 2021, pp. 143–174. doi:10.1016/B978-0-12-819994-7.00011-X.

[26] J. S. Orr, T. M. Barrows, C. W. Russell, R. K. Moore, A. Alaniz, S. G. Ryan, Advanced Modeling of Control-Structure Interaction in Thrust Vector Control Systems, in: 45th Annual AAS Guidance, Navigation and Control (GN&C) Conference, Breckenridge, CO, 2023. URL: https://ntrs.nasa.gov/citations/20230000427.

[27] M. Otter, H. Elmqvist, S. E. Mattsson, The New Modelica MultiBody Library, in: 3rd International Modelica Conference, 2003, p. 21.

[28] J.-C. Mare, Friction modelling and simulation at system level: A practical view for the designer, Proceedings of the Institution of Mechanical Engineers, Part I: Journal of Systems and Control Engineering 226 (2012) 728–741.

[29] J.-C. Maré, Friction modelling and simulation at system level: Considerations to load and temperature effects, Proceedings of the Institution of Mechanical Engineers, Part I: Journal of Systems and Control Engineering 229 (2015) 27–48.

[30] J.-C. Maré, Practical Considerations in the Modelling and Simulation of Electromechanical Actuators, Actuators 9 (2020) 94.

[31] J.-C. Maré, Requirement-based system-level simulation of mechanical transmissions with special consideration of friction, backlash and preload, Simulation Modelling Practice and Theory 63 (2016) 58–82.

[32] L. Wang, J.-C. Maré, A force equalization controller for active/active redundant actuation system involving servo-hydraulic and electromechanical technologies, Proceedings of the Institution of Mechanical Engineers, Part G: Journal of Aerospace Engineering 228 (2014) 1768–1787.

[33] J. Fu, Incremental Virtual Prototyping of Electromechanical Actuators for Position Synchronization, Doctoral thesis, Université de Toulouse, Toulouse, France, 2016.

[34] J. Fu, J.-C. Maré, Y. Fu, Modelling and simulation of flight control electromechanical actuators with special focus on model architecting, multidisciplinary effects and power flows, Chinese Journal of Aeronautics 30 (2017) 47–65.

[35] C. Renault, Usefulness of a force feedback on electromechanical actuator, in: 6th International ESA Conference on Guidance, Navigation and Control Systems, Loutraki, Greece, 2005.

[36] L. E. Briese, P. Acquatella B, K. Schnepper, Multidisciplinary modeling and simulation framework for launch vehicle system dynamics and control, Acta Astronautica 170 (2020) 652–664.

[37] J. L. R. Gutierrez, S. Farì, M. Winter, Control System Design for the ALINA Lunar Lander, in: Proceedings of the International Astronautical Congress, volume A3, Dubai, UAE, 2021.

[38] G. Looye, The New DLR Flight Dynamics Library, in: 6th Modelica Conference, Bielefeld, Germany, 2008, p. 10.

[39] T. Pulecchi, F. Casella, M. Lovera, A Modelica Library for Space Flight Dynamics, in: 5th International Modelica Conference, 2006, p. 10.

[40] F. van der van der Linden, C. Schlegel, M. Christmann, G. Regula, C. Hill, P. Giangrande, J.-C. Maré, I. Egaña, Implementation of a Modelica Library for Simulation of Electromechanical Actuators for Aircraft and Helicopters, in: The 10th International Modelica Conference, March 10-12, 2014, Lund, Sweden, 2014, pp. 757–766. doi:10.3384/ecp14096757.

[41] S. Bozhko, C. Hill, P. Giangrande, C. Gerada, A Novel Multi-Level Electro-Mechanical Actuator Virtual Testing and Analysis Tool, in: 7th IET International Conference on Power Electronics, Machines and Drives (PEMD 2014), Institution of Engineering and Technology, Manchester, UK, 2014, pp. 0249–0249. doi:10.1049/cp.2014.0360.

[42] S. E. Mattsson, H. Elmqvist, M. Otter, Physical system modeling with Modelica, Control Engineering Practice 6 (1998) 501–510.

[43] Modelica Association, Modelica 3.4- A Unified Object-Oriented Language for Systems Modeling. Language Specification, 2017. URL: https://modelica.org/documents/ModelicaSpec34.pdf.

[44] Modelica Association, Modelica Standard Library, Modelica Association, 2021. URL: https://github.com/modelica/ModelicaStandardLibrary.

[45] F. Al-Bender, Fundamentals of friction modeling, in: ASPE Spring Topical Meeting on Control of Precision Systems, volume 48, ASPE-The American Society of precision Engineering, Cambridge (MA), USA, 2010, pp. 117–122.

[46] M. Nordin, P.-O. Gutman, Controlling mechanical systems with backlash—a survey, Automatica 38 (2002) 1633–1649.

[47] R. Krishnan, Permanent Magnet Synchronous and Brushless DC Motor Drives, 1 ed., CRC Press, Boca Raton (FL), USA, 2017. doi:10.1201/9781420014235.

[48] P. C. Krause, O. Wasynczuk, S. D. Sudhoff, S. Pekarek, Analysis of Electric Machinery and Drive Systems, IEEE Press Series on Power Engineeering, third edition ed., Wiley, Hoboken (NJ), USA, 2013.

[49] P. Simplicio, Guidance and Control Elements for Improved Access to Space, Ph.D. thesis, The University of Bristol, 2019. URL: https://research-information.bris.ac.uk/en/studentTheses/guidance-and-control-elements-for-improved-access-to-space.

[50] M. Illig, S. Ishimoto, E. Dumont, CALLISTO, a demonstrator for reusable launchers, in: 9th European Conference For Aeronautics And Space Sciences (EUCASS), 2022. doi:10.13009/EUCASS2022-7239.

[51] M. Sagliano, T. Tsukamoto, A. Heidecker, J. M. Hernández, S. Farì, M. Schlotterer, S. Woicke, D. Seelbinder, S. Ishimoto, E. Dumont, Robust Control for Reusable Rockets via Structured H-inf Synthesis, in: 11th International ESA Conference on Guidance, Navigation & Control Systems, 2021.

[52] C. Pelchen, C. Schweiger, M. Otter, Modeling and Simulating the Efficiency of Gearboxes and of Planetary Gearboxes, in: Proceedings of 2nd International Modelica Conference, Oberpfaffenhofen, Germany, 2002, pp. 257–266. URL: https://elib.dlr.de/11828/.